

Structural geology using borehole-wall imagery: Case studies of 3 HiRAT logs.

Andrew W.B. Siddans & Paul R. Worthington, Robertson Geologging Ltd., Deganwy, Conwy LL31 9PX, UK.

1. Introduction

Processing and interpretation of Acoustic Televiwer (HiRAT) logs is described. The featured boreholes are:

1. TB10, logged interval 4.313-61.214m, nominal diameter 76mm, maximum deviation 2.3°, in granites (South Korea). The log was acquired for SEKOGEO Co. Ltd., as part of a geotechnical site investigation.
2. Brigadoon2, logged interval 1039.680-1204.920m, nominal diameter 76mm, maximum deviation 7.4°. The log was acquired as part of a geotechnical site investigation.
3. Deganwy borehole, logged interval 29.993-90.001m, nominal diameter 112mm, maximum deviation 12.0°, in Ordovician volcanics (North Wales), the RG test borehole.

The HiRAT sonde uses a fixed acoustic transducer and rotating mirror system to acquire 2-way travel-time and amplitude of the acoustic signal reflected back to the transducer from a spiral trajectory on the borehole-wall. The pitch of the spiral depends on logging speed and rotation-rate of the mirror. The depth of the start of each spiral was recorded at 1mm resolution, amplitude/travel-time data was recorded at 2° intervals around each spiral. The start of each spiral is referenced to Magnetic North during acquisition, using data from the 3-axis magnetometer-accelerometer unit in the sonde.

Borehole TB10 was lined with grey PVC casing to a depth of 11.2m, then with transparent-acrylic casing from 11.2 - 30.2m, below which the borehole is open. Traces of various geologic features are recorded on the imagery, among which, with the aid of an accompanying Optical Televiwer (OPTV) log, fractures, quartz-veins and darker veins can be identified. The quality of both the HiRAT and OPTV imagery in the transparent-acrylic casing is surprisingly good. It introduces a decrease in overall amplitude and a faint, sub-vertical, background pattern on the amplitude image, on which the geologic information is superposed (Fig. 1). Geologic features are very much more evident on the travel-time image in the transparent-acrylic, cased section than elsewhere, an unexpected effect for which we can offer no real explanation.

Processing of such imagery includes:

1. Rasterization of the spirally-distributed log data onto a rectangular grid.
 2. Identification of zones affected by magnetic anomalies and correction of corresponding anomalous sonde orientation data.
 3. Determination of the trajectory of the borehole-axis in 3D space.
 4. Identification of any irregularities in the borehole-wall (breakout phenomena) that may be indicative of high deviatoric stress.
 5. Creation of a decentralization-corrected version of the amplitude image for feature-picking purposes, if necessary.
 6. Identification and labelling of significant geologic features along with their orientation and depth on the borehole-axis.
- Methods and results are described in the Processing section below.

Fracture Analysis of the dips resulting from processing aims to identify geometric sets of fractures/veins, then estimate variations in mean-dip and frequency within the sets and lines of intersection among the sets, with depth. The frequency data is used to calculate a Volumetric joint count log, from which a Rock quality designation log can be estimated. In sedimentary terrains Structural Interpretation aims to extract formation dip and identify geologic structures such as unconformities, folds and faults, from the distribution and orientation of dips assigned to bedding. Methods and results are described in the Interpretation section below.

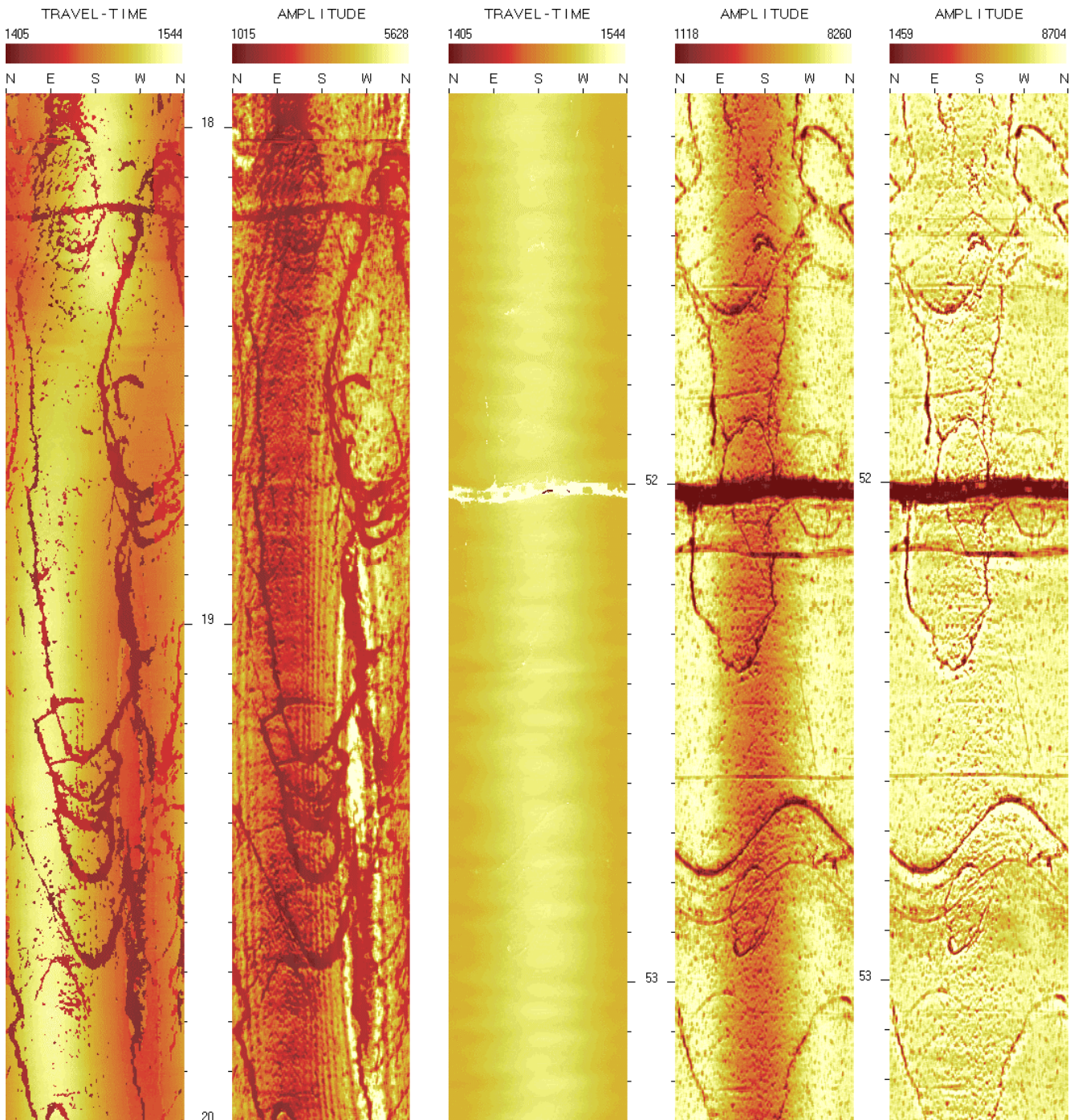


Fig. 1: Sections of HiRAT log in transparent-acrylic casing (17.9 -20.0 m) and open hole (51.2 -53.3m). Travel-time units are $0.1\mu\text{sec}$, Amplitude is dimensionless. A decentralization-corrected version of the 51.2 - 53.3m amplitude image is shown on the far right. Borehole TB10.

2. Processing

a. Rasterization of the log data

The 1st stage in Acoustic televiewer processing (data input and pre-processing stage) is to interpolate the spirally-distributed travel-time/amplitude data onto a rectangular grid with axes azimuth v depth. The n° azimuth increment, selected for logging is retained, the optimum depth increment for interpolation depends on logging speed, in these logs it is 2mm. All subsequent processing is done on the rasterized data. The dynamic ranges of travel-time and amplitude values in the rasterized imagery are determined at this stage and used subsequently to optimize use of a 256-color palette for displaying the imagery.

b. Magnetic anomaly identification and correction

Sonde orientation is calculated from the magnetometer-accelerometer data, at twice the depth interval in the rasterized image, throughout the log, during pre-processing. The calculated parameters include Magnetic Tool Face (MTF), Relative Bearing (RB) and Sonde-axis deviation from the vertical. Sonde-axis deviation azimuth = MTF-RB. The solid angle between the earth's gravity and magnetic fields (G^H) is also calculated. This angle is very stable in the absence of magnetic anomalies and sections of log where it becomes unstable provide a good indicator of their presence. Variation of G^H with depth in borehole TB10 (non-metallic casing) is compared with that in the Deganwy borehole (metallic casing) in Fig. 2.

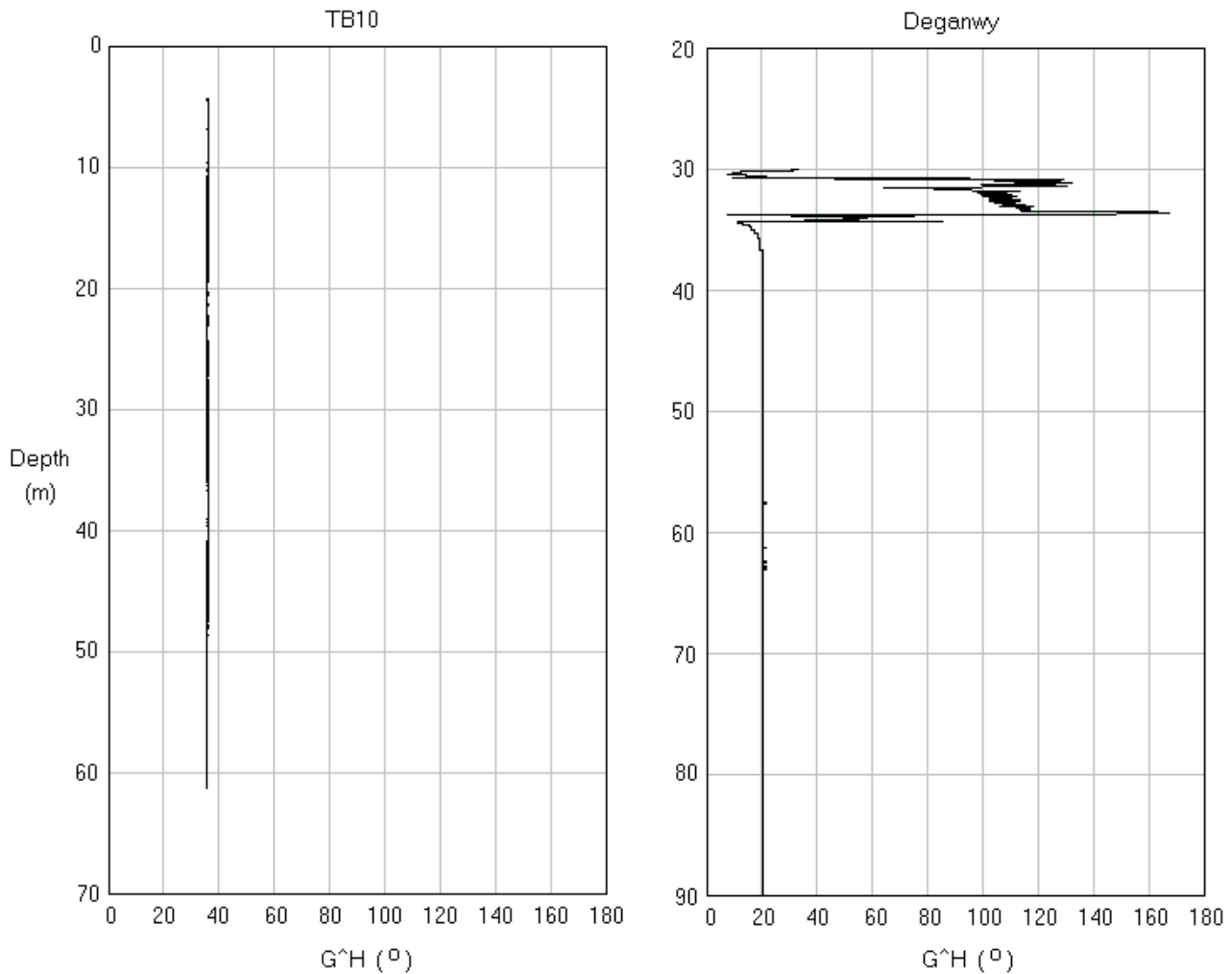


Fig. 2: Variation of solid angle G^H with depth in HiRAT logs of boreholes with non-metallic casing down to 30.2m (TB10) and metallic casing down to 32m (Deganwy).

If magnetic anomalies are detected, as in the case of the Deganwy borehole, where metallic casing down to 32m produces anomalies down to 36m in the HiRAT log, sonde orientation data and image alignment to magnetic North will both be wrong. Various correction techniques are available:

1. If an independent borehole deviation survey is available from a sonde that does not rely on the earth's magnetic field, e.g. Gyro, Fotobor or Maxibor, the difference in deviation azimuth data from the HiRAT data can be used to correct the anomalous orientation data from the HiRAT log.
2. Individual zones of anomalous orientation data can be corrected by extrapolating orientation angles over this interval, using values from selected depths below (and above) the anomalous zone. Use of this technique is illustrated for the Deganwy borehole in Fig. 3.

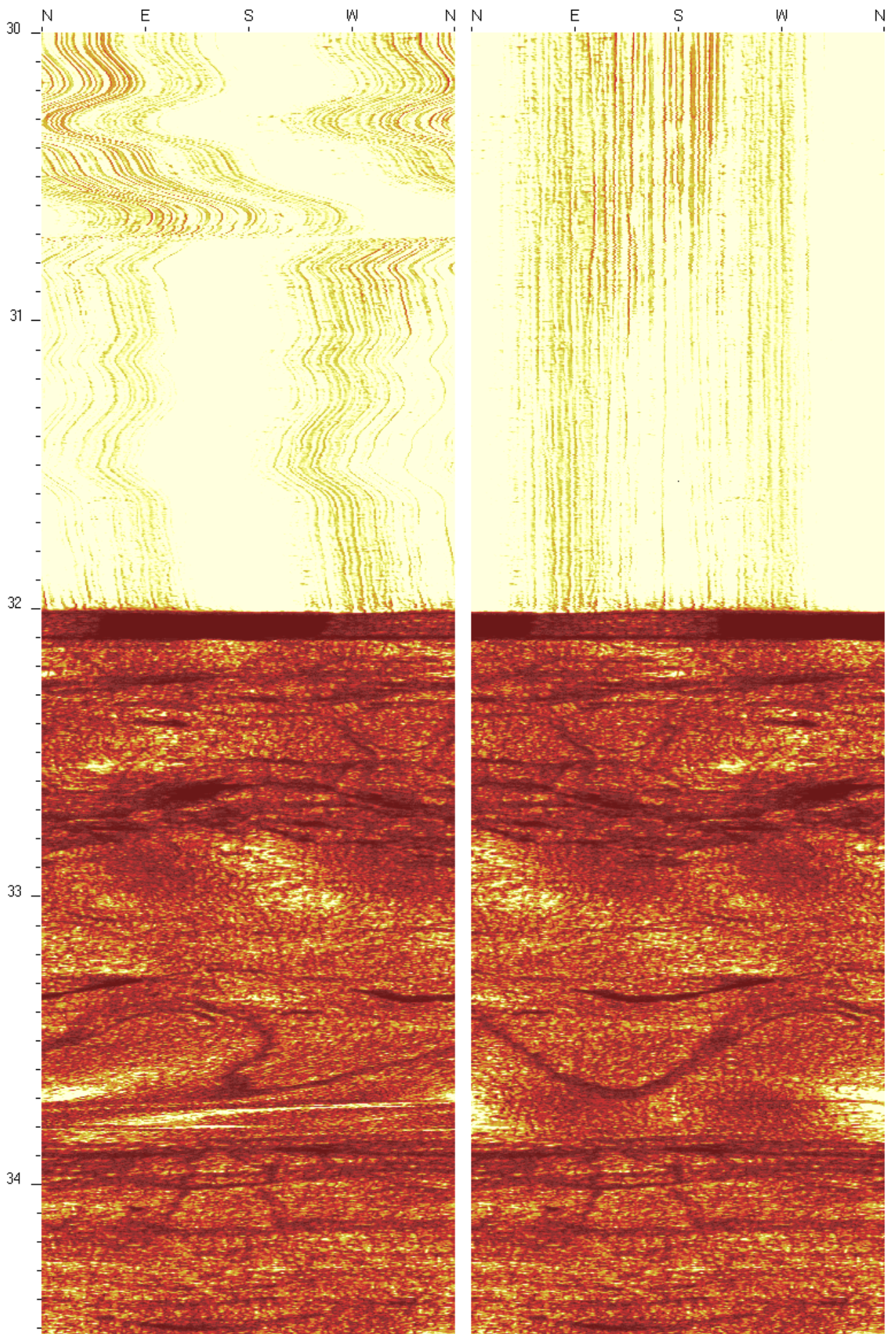


Fig. 3: Deganwy borehole HiRAT amplitude image, before and after correction for magnetic anomalies.

Both of these techniques work fine for correction of borehole deviation data, but successful correction of image orientation to magnetic North can only be achieved when borehole deviation magnitude from vertical exceeds a few degrees. No magnetic anomalies are indicated in HiRAT log TB10.

c. Borehole deviation

Borehole trajectories are calculated by integrating individual borehole deviation estimates, at regular intervals on the borehole-axis, down the log (Fig. 4).

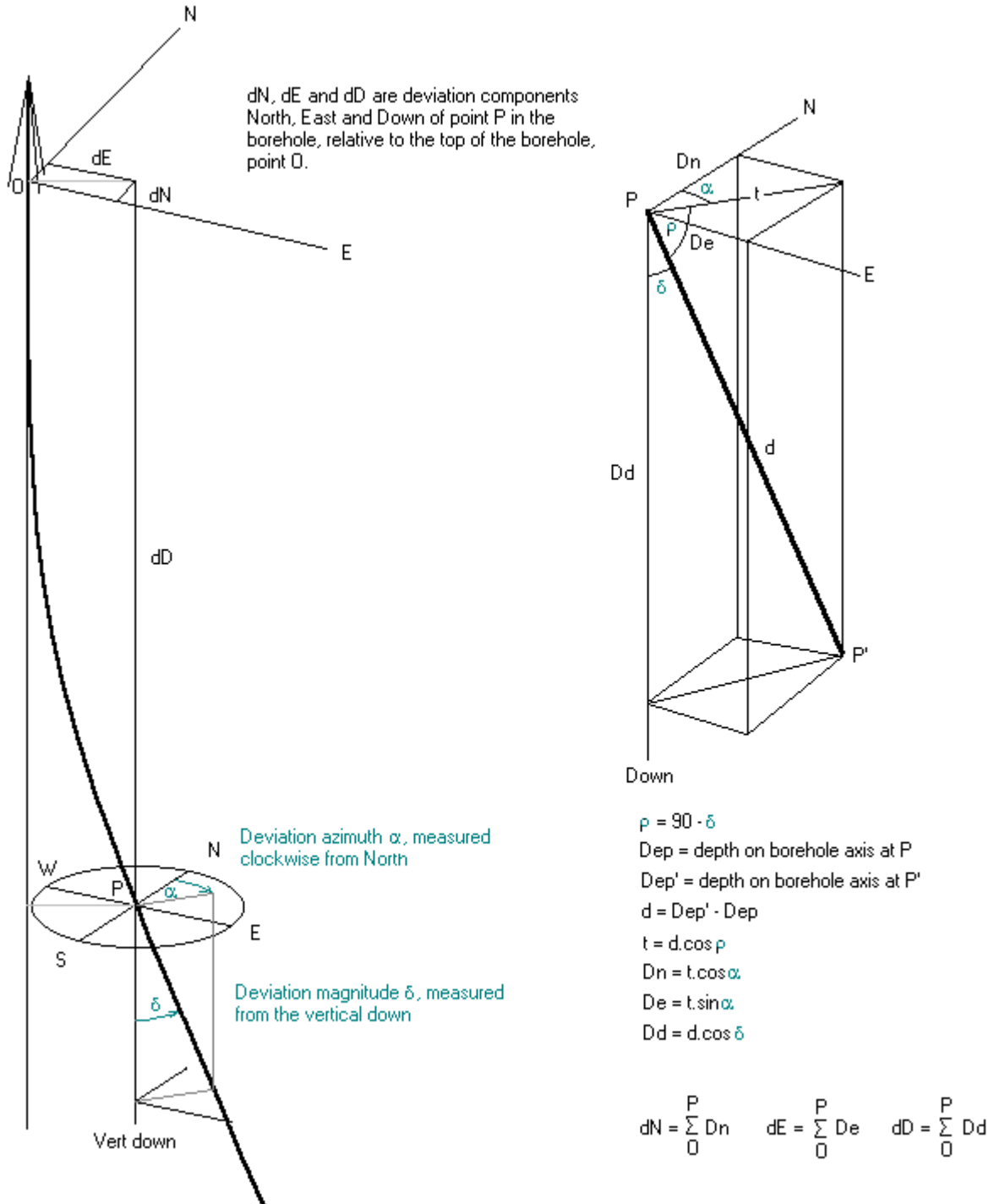


Fig. 4: Calculation of deviation components North, East and Down, in an inclined borehole.

It is tacitly assumed that borehole-axis orientation = sonde-axis orientation at all individual data points on the borehole-axis. This may be achieved by good sonde centralization in approximately vertical boreholes, but in inclined boreholes it is an act of faith. The HiRAT sonde is 1.98m long and without centralizers has diameter 45mm. These dimensions and borehole diameter fix limits to the worst-case possible tilt of sonde-axis relative to borehole-axis (Fig. 5).

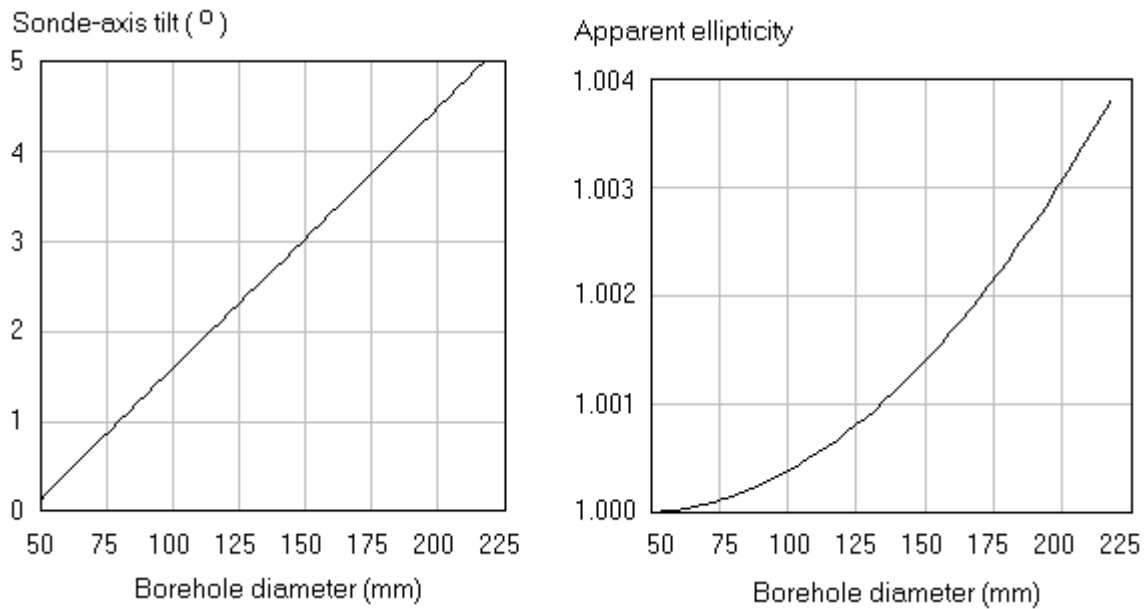


Fig. 5: Variation in worst-case possible tilt of HiRAT sonde-axis relative to borehole-axis and resulting apparent borehole ellipticity, with borehole diameter.

Results of a borehole deviation analysis are typically presented as a 3D view of the borehole in orthographic projection (Fig. 6a) and projections of the trajectory onto vertical N-S and E-W planes and a horizontal plane (Fig. 6b). If deviation data is extrapolated to the surface and top of the borehole coordinates (North, East and Elevation) are input, the accompanying tabulated data includes calculated borehole-axis coordinates. Borehole TB10 is almost vertical, the bottom of the borehole is displaced horizontally from the top by only 0.542m.

When several boreholes have been processed in the same field, cross-hole azimuth/distance data can be calculated and tabulated with depth or elevation.

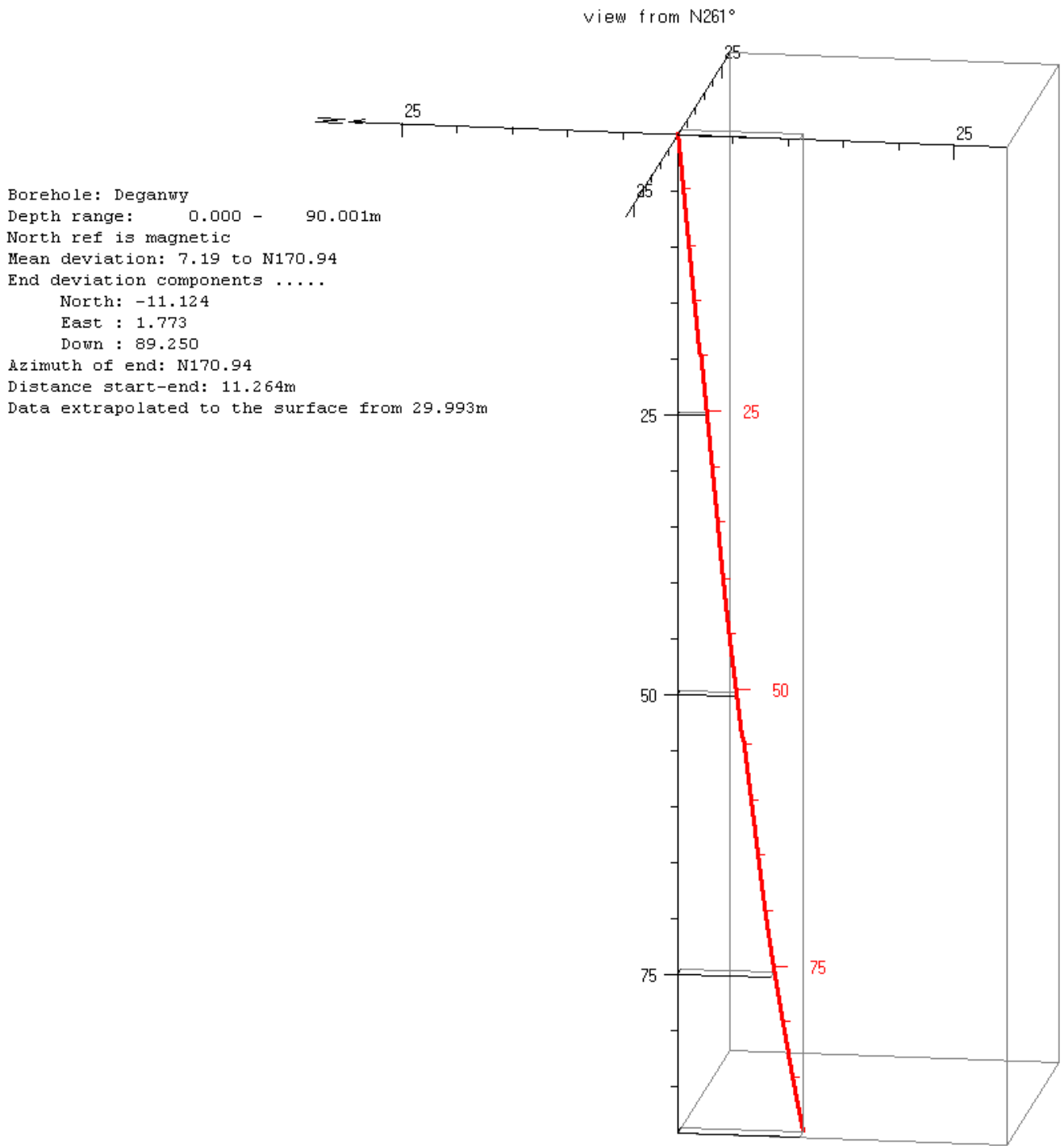


Fig. 6a: Deganwy borehole viewed in 3D orthographic projection. The depth-scale in red shows log depths, measured down the borehole-axis.

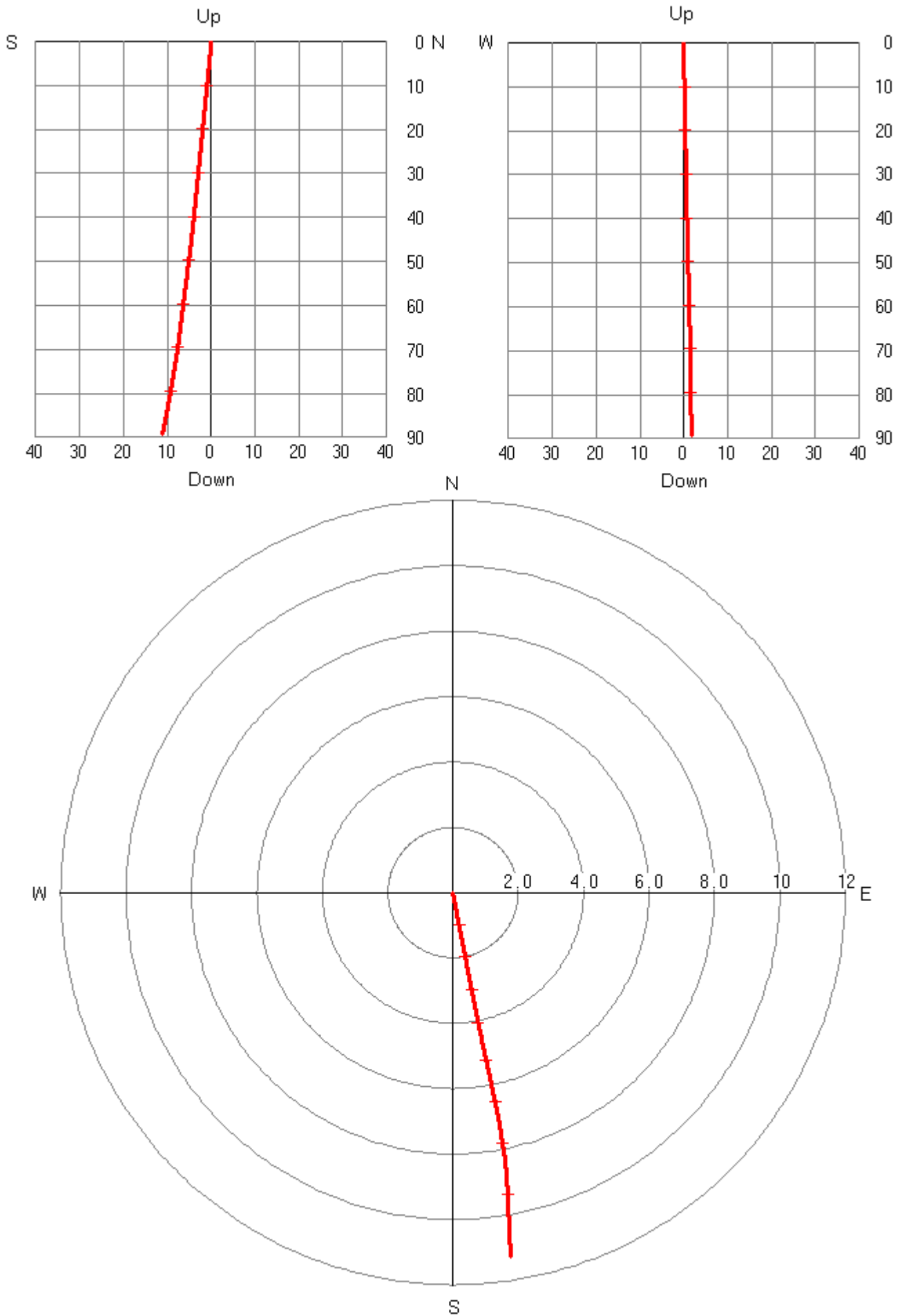


Fig. 6b: Vertical N-S and E-W and enlarged horizontal projections of the Deganwy borehole. Scales in m.

d. Sonde decentralization and Breakout/Ovalization

In terrains of high regional stress, the fact of drilling a borehole introduces a cylindrical, fluid-filled hole. The fluid does not support shear stress and stress trajectories in the vicinity of the borehole are distorted so that they become parallel and perpendicular to the borehole-wall. Where stress trajectories converge deviatoric stresses increase and may result in borehole-wall instability, manifesting itself typically as a pair of breakout bands on diametrically opposite sides of the borehole-wall. The HiRAT travel-time log can be used to construct a 3D model of the borehole-wall, by stacking up successive borehole cross-sections, providing a reasonable estimate of acoustic velocity in the borehole fluid is available. If a caliper log is available a usable fluid velocity profile can be created from the travel-time log. An integral stage in construction of the cross-sections is to estimate the position of the sonde in the borehole, using radii calculated from the travel-time data and a method of moments technique.

Breakouts are identified as diametrically opposed pairs of bands with high travel-times and low amplitude, parallel to the borehole-axis, on the HiRAT amplitude/travel-time log. The high travel times result from longer acoustic paths into the sectors where the borehole-wall has broken away, the lower amplitudes result from the acoustic beam intersecting the broken borehole-wall obliquely in these sectors. An example, at 1077-1078m depth in the Brigadoon2 borehole, is shown in Fig. 7.

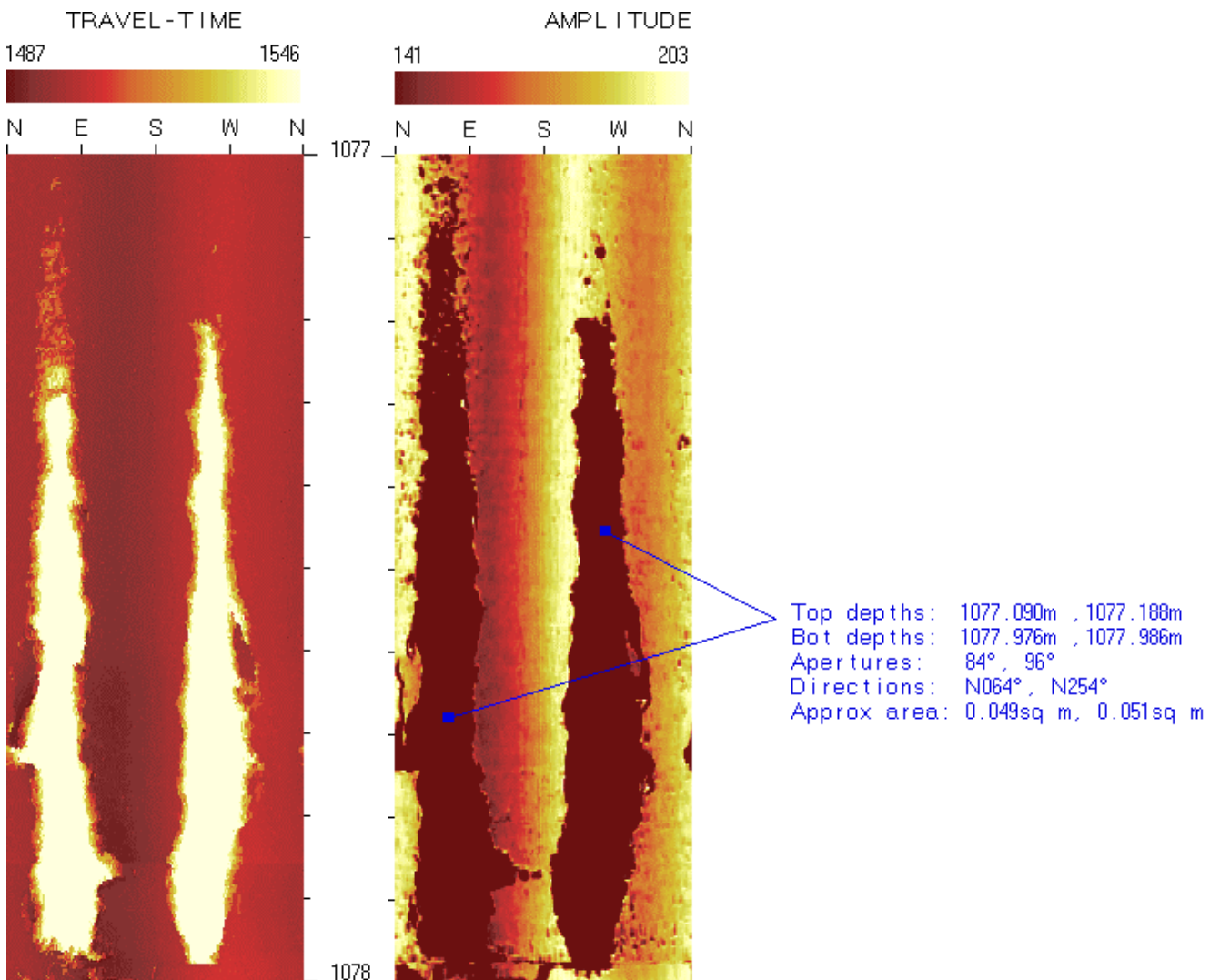
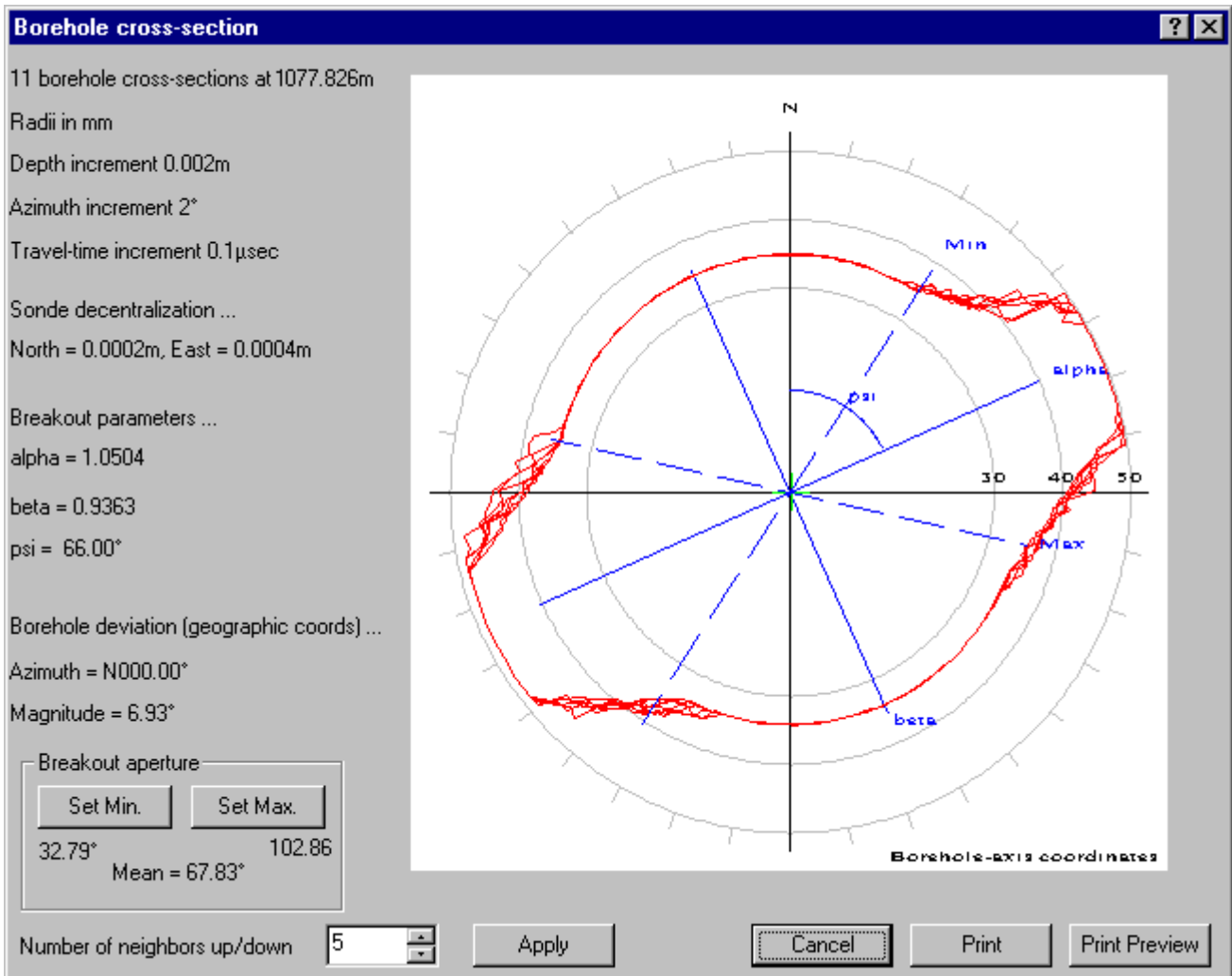


Fig. 7: Diametrically opposed breakout bands in the Brigadoon2 borehole.

The breakout annotations give an overall summary of the breakout geometry, obtained by digitizing top, bottom, left and right points on each band. More accurate parameters can be obtained by inspection of borehole cross-sections at selected depths (Fig. 8). Of particular interest from a rock mechanics point of view is the mean breakout direction and the angular aperture of the breakout sector.



ig. 8: 11 superposed borehole cross-sections, 1077.816 - 1077.836m, through the breakout bands in the Brigadoon2 borehole shown in Fig. 7. Digitized breakout aperture extends from N032.8° (Min) - N102.9° (Max), with mean direction N067.8°. The major axis (alpha) of the best-fit elliptical cross-section is oriented N066.0° (psi).

In contrast to the Brigadoon2 borehole, no breakout bands are seen in the amplitude/travel-time log for borehole TB10 (Fig. 1) and borehole cross-sections are circular (Fig. 9). Sonde decentralization in both examples is very small, 0.47mm/N063.4° in the Brigadoon2 borehole (Fig. 8), 0.8mm/N000.0° in borehole TB10 (Fig. 9). The acoustic transducer and mirror are situated near the bottom of the HiRAT sonde, when at least the bottom of the sonde is well-centralized in a borehole the worst-case possible tilt angles of sonde-axis relative to borehole-axis, shown in Fig. 5, can be halved. Outside of the breakout sectors in the Brigadoon2 borehole, cross-sections for both boreholes are circular. This also indicates that sonde-axis parallels the borehole-axis in both boreholes.

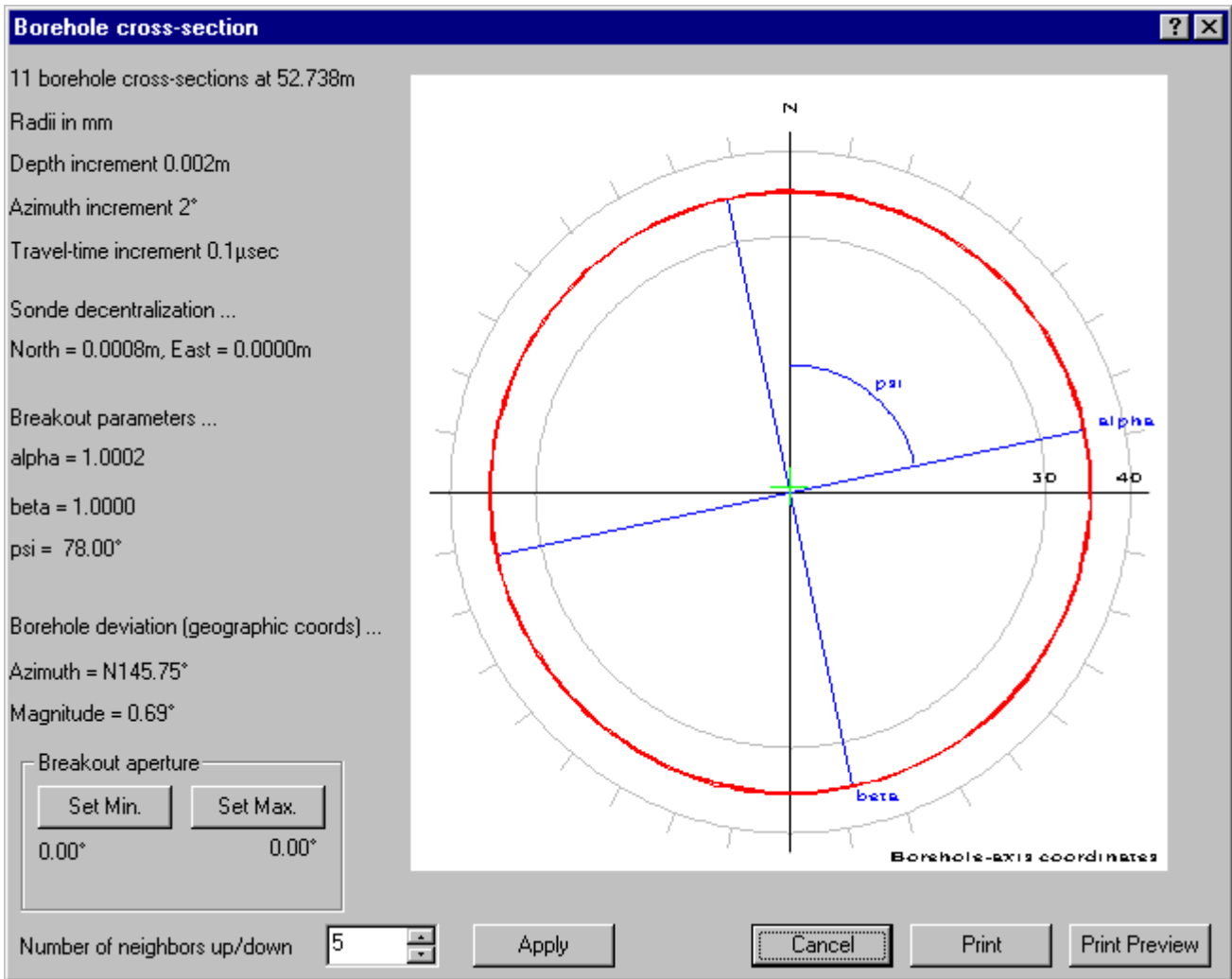


Fig. 9: 11 superposed borehole cross-sections, 52.728 - 52.748m, through circular borehole TB10 shown in Fig. 1.

e. Decentralization-corrected amplitude image

If a single dark vertical band appears in the amplitude image background, opposite to the brightest band, with corresponding bands of higher and lower values on the travel-time image, a small amount of sonde decentralization is indicated. This results from decrease in acoustic pressure with increase in acoustic path length (see Appendix I).

Higher amounts of sonde decentralization result in a pair of dark bands, with intervening bright bands, on the amplitude image. One of the bright bands corresponds with the direction of decentralisation, the other is at $+180^\circ$. The dark bands arise from the acoustic beam intersecting the borehole-wall obliquely in the intervening sectors (see Appendix II).

These dark bands become a nuisance when they obscure geologic detail on the imagery. In particular they reduce amplitude-gradients across parts of the image, which detracts from the extent to which individual sinusoidal traces of features can be identified automatically or semi-automatically. If this is the case it is worth creating a decentralization-corrected amplitude image for feature-picking purposes. Fig. 1 (far right) shows the decentralization-corrected version of the 51.2-53.3m section of amplitude image for borehole TB10.

Correction of the amplitude image for sonde decentralization requires consideration of the geometry of the HiRAT acoustic beam. Zemanek (1971), in a landmark paper, showed how to calculate the distribution of pressure in the acoustic beam produced in a fluid by a flat, circular transducer of known characteristics. The same calculations, with extensions to include concave and 'Gaussian' transducers, have been programmed to investigate various transducer configurations, including that eventually used in the HiRAT sonde. An outline of this is given in Appendix I, decentralized HiRAT logs are discussed in Appendix II.

f. Feature-picking

Planar geologic features intersecting a circular borehole obliquely leave fixed-period, sinusoidal traces on the unrolled borehole-wall image (Fig. 10a,b).

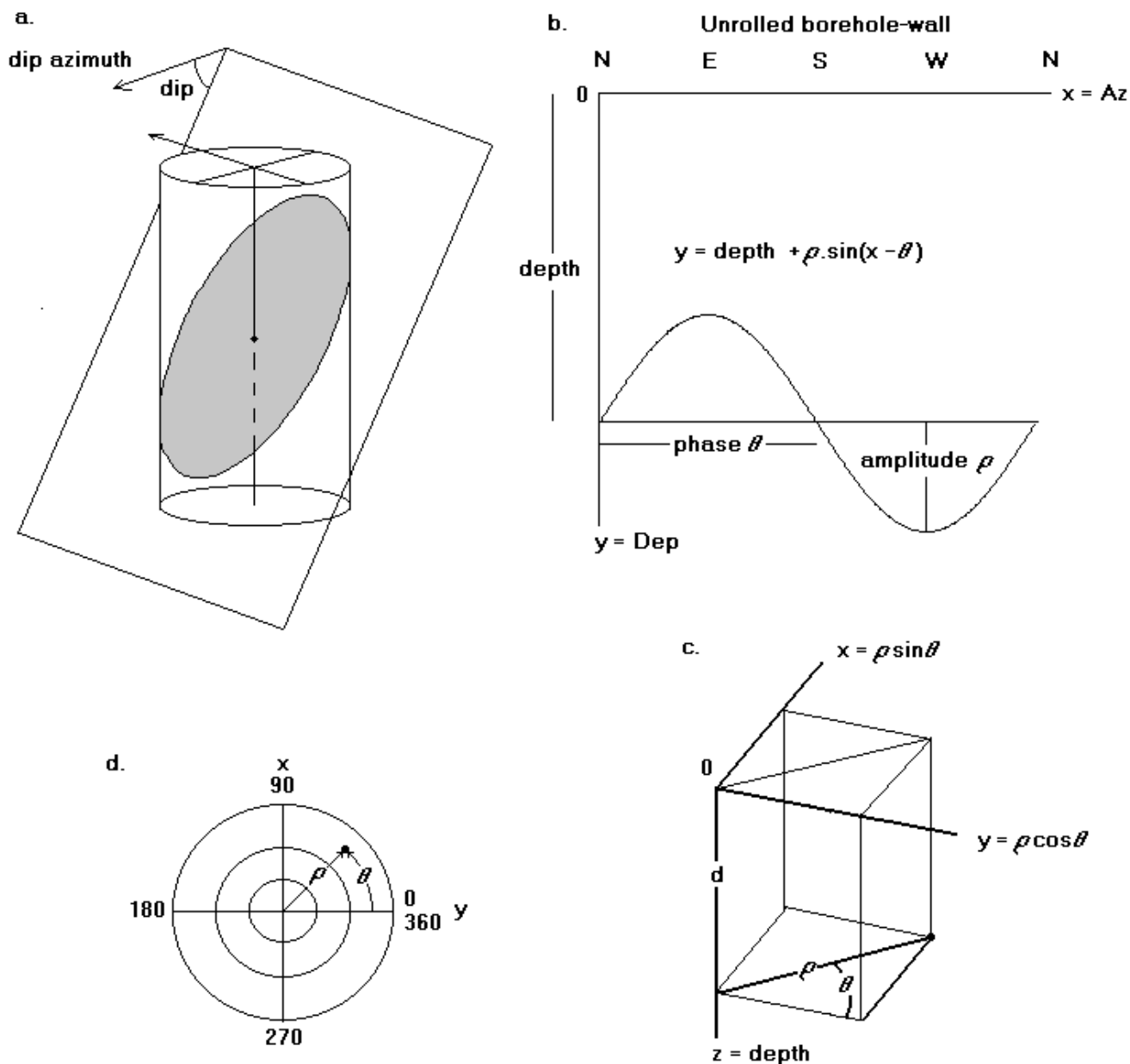


Fig. 10: a: Plane intersecting a cylindrical borehole obliquely. b: Sinusoidal trace of oblique plane on the unrolled borehole-wall image. c: 3D Hough space used for characterisation of fixed-period sinusoids. d: Hough transform map (xy-section) at depth *d*.

When borehole diameter and borehole-axis orientation are known, the dips of features can be calculated from the phase and amplitude of their sinusoidal traces. Classic techniques for estimating phase and amplitude are interactive: individual points can be picked on a trace and the necessary trigonometric calculations made, or a flexible sinusoid dragged into position above the trace. Both these techniques are well tried and tested and work fine. They are, however, time-consuming, require great concentration and accuracy with the mouse.

Inspection of any reasonably exposed outcrop soon reveals that veins and fractures are not continuous. Frequently they terminate at bed boundaries, or against veins or fractures of a different geometric set. Some geologic environments are typified by discontinuous beds, veins or fractures in characteristic patterns, *e.g.* truncated units in cross-bedded sandstones, en-echelon patterns in shear-zones, or sets of discontinuous fractures on diagonally-opposite sides of a borehole in terrains of high deviatoric stress. In addition to identification of individual features and dip calculation, intersection relationships among the features should be recorded by the processing. This can be largely achieved by storing the azimuths of the limits of up to 3 segments on the borehole-wall image.

Glossop *et al.* (1997, 1999) describe a method for semi-automatic feature-picking on Acoustic Televiewer (BHTV) imagery, which was subsequently extended to OPTV imagery. Siddans (2002) outlined a fully-automatic feature-picking

method, illustrated with an example from an OPTV log in flagstones from N. Scotland. This is all based on a Hough transform technique, using parameters:

$$x = \rho \cdot \sin\theta$$

$$y = \rho \cdot \cos\theta$$

$$z = \text{depth}$$

where ρ = sinusoid amplitude and θ = sinusoid phase.

Individual sinusoids, plotted in 3D Hough space, give rise to bi-conical shapes, forming a bright spot at the apex. The x,y,z-coordinates of the bright spot fix the sinusoid's depth, amplitude and phase, which can be converted into dip and dip-azimuth (Fig. 10c,d).

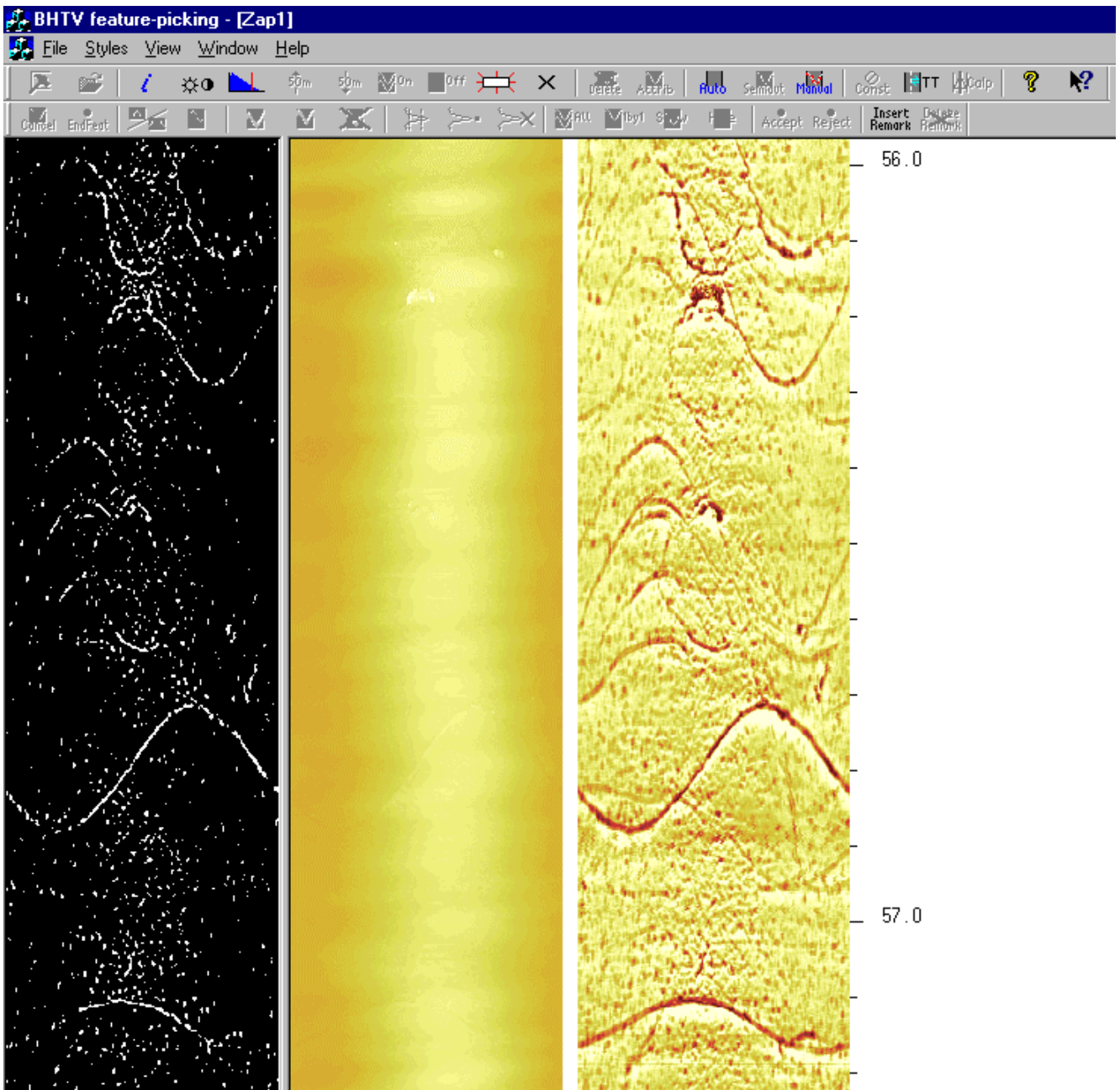


Fig. 11: Section of the TB10 HiRAT log, ready for semi-automatic or automatic feature-picking. The decentralization-corrected amplitude image is shown.

Details of the methods used to extract sinusoidal shapes from BHTV and OPTV imagery are given by Glossop *et al.* (1997, 1999) and Siddans (2002). In summary, in the case of BHTV imagery this is done by converting the amplitude image to a binary, amplitude-gradients image by edge-detection, using a Laplacian of Gaussians (LoG) filter with a 3x3 input window, with a variable threshold under user control. The aim is to set a threshold value that shows the main features as white, sinusoidal traces, without too much white, background noise. If you can see white sinusoids on the binary, amplitude-gradients image you can detect them semi-automatically or automatically. The resulting dip is derived

objectively, exclusively from information contained in the image. It can be repeated many times over and you get exactly the same result.

A section of the TB10 HiRAT log is shown in the feature-picking window in Fig. 11, with the binary amplitude-gradients image in the left pane and the decentralization-corrected amplitude image in the right pane, ready for semi-automatic or automatic feature-picking.

i. Semi-automatic feature-picking

In this mode 2 points are picked approximately in the region of the crest and trough of a sinusoidal trace. These fix the depth, phase and amplitude of a seed-point in 3D Hough space, which becomes the centre of a surrounding search-cube. A search-range is defined in terms of the depth spacing in the rasterized image, which determines the maximum sinusoid amplitude that will be detected. For a given borehole diameter this effectively defines the maximum dip (in well-axis coordinates) that will be detected, *cf.* the search angle as used in Dipmeter interval correlation.

Each point (x,y,z) in the search-cube represents a different sinusoid in terms of phase, amplitude and depth. Each point (Az,Dep) on the binary gradients-image, within the depth-range defined by the search-cube and the search-range can belong to one of these sinusoids. The search for sinusoids algorithm loops through all points (x,y,z) in the search-cube. At each it looks at each point (Az,Dep) on the binary gradients-image that belongs to the sinusoid represented by point (x,y,z). If point (Az,Dep) on the binary gradients-image is represented by a white pixel, the current point (x,y,z) in the search-cube gets one vote. It is a democratic process, the point in the search-cube getting the most votes wins and is declared to be the best sinusoid for the initial seed-point. In many ways the procedure is analogous to the global mapping technique used in Dipmeter interval correlation.

ii. Fully-automatic feature-picking

In this mode there is a search-range, defined as in the case of semi-automatic feature-picking, centred on the current processing depth. The complete procedure works in 3 stages:

1. The search-range is moved up the complete log, in increments of the log depth-spacing, creating a Hough transform map for that depth. At each depth (z) the algorithm loops through all points (x,y) within the search-range, then looks at each point (Az,Dep) on the binary gradients-image that belongs to the sinusoid represented by point (x,y,z). If the point (Az,Dep) on the binary gradients-image is represented by a white pixel, the current point (x,y,z) in the Hough transform map gets one vote. Depth, maximum value on the Hough transform map and its x,y-coordinates are stored as an Autofeats log (Fig. 12). This stage is time-consuming, but requires no user-intervention and can be run silently in the background.
2. Data from the Autofeats log is used to construct a graph of maximum Hough transform map values v depth, which is displayed alongside the binary gradients-image (Fig. 13). A feature-seeking algorithm moves up this graph looking for peaks, converting these into sinusoids and superposing them on the binary gradients-image. A number of filters can be used in converting peaks into sinusoids, including peak-size, automatic elimination of straight features perpendicular to the borehole-axis and a test to check that peaks on the graph correspond to apices of bi-conical shapes in the 3D Hough space. An automatic sinusoid segmentation algorithm can also be used to delimit the extent of segments of discontinuous features. These filters can be selected, deselected or changed on a trial and error basis, to optimise the fit of the traces of calculated sinusoids to those on the binary gradients-image. Further peaks can be selected interactively to create new sinusoids, peaks with sinusoids that do not correspond with traces on the binary gradients-image, can be eliminated interactively.
3. There are 2 options for labelling the sinusoids identified at stage 2. The simplest assigns the same set of attributes to all features in a single operation, the other displays the amplitude/borehole-wall image and moves up the log superposing the sinusoids 1 by 1, so that attributes can be applied individually.

The log is left with all features drawn on the amplitude/borehole-wall image, with calculated dips and labels displayed alongside (Fig. 14). It is in semi-automatic feature-picking mode for addition of more features that escaped fully-automatic processing, segmentation or addition of thickness to existing features, editing or deletion of features incorrectly processed by the fully-automatic mode.

Finally, manual feature-picking mode can be selected to finish processing those features that can not be done in semi-automatic mode. The effects of sonde decentralization on calculated dips is discussed in Appendix III.

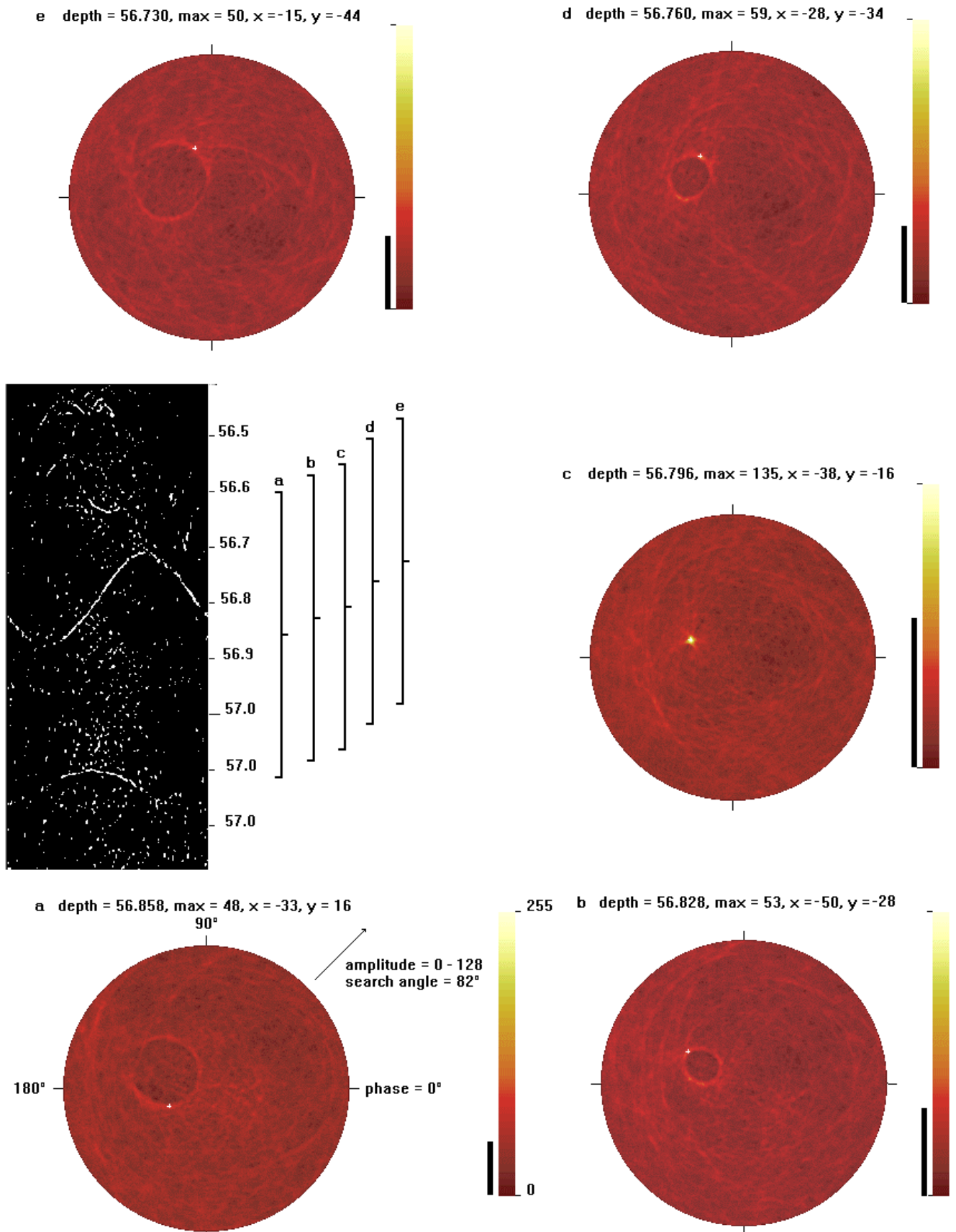


Fig. 12: Hough transform maps at successive depths as the processing depth moves upwards through the sinusoidal feature at 56.796m in borehole TB10.

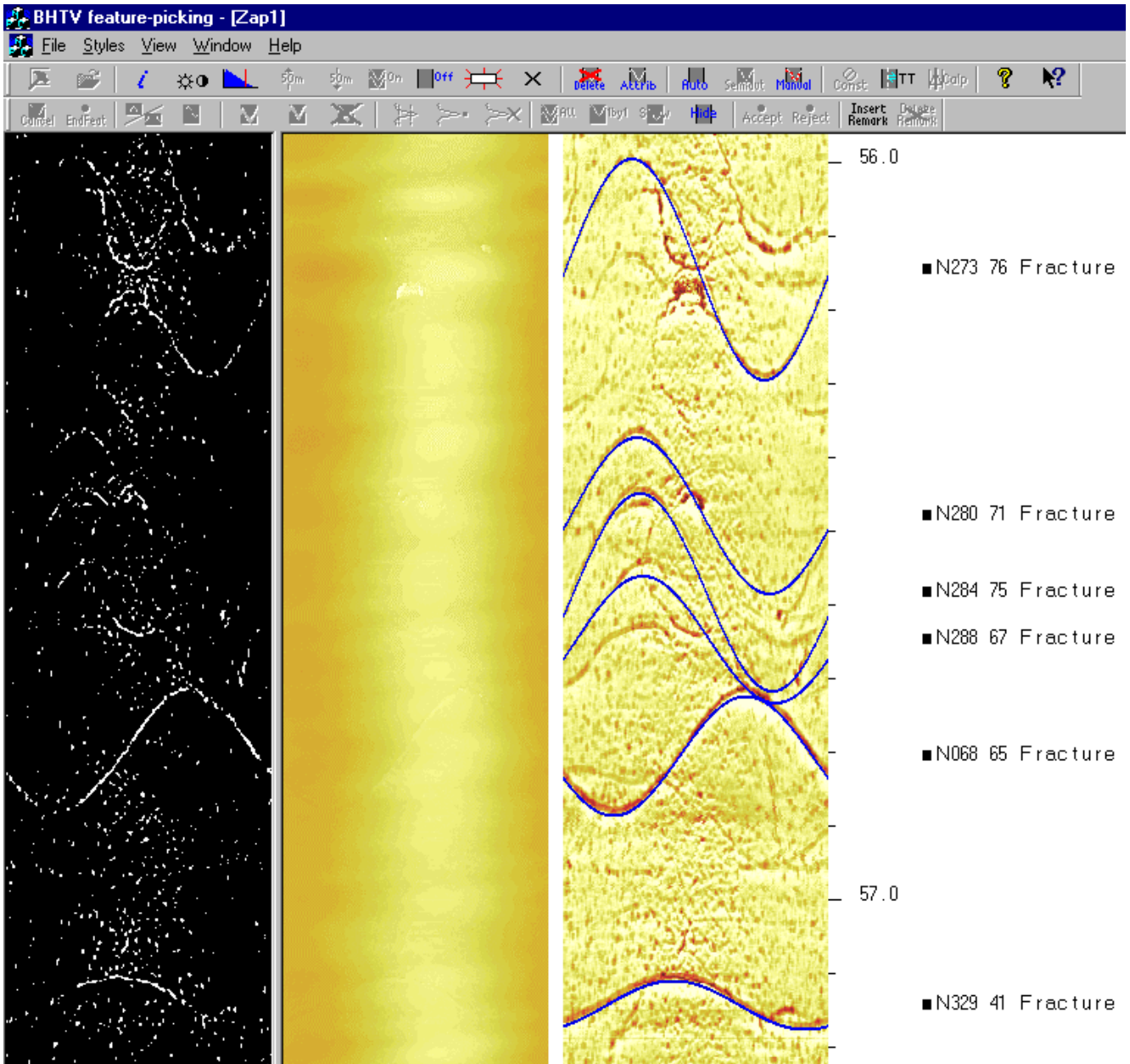


Fig. 14: The sinusoids identified by fully-automatic feature-picking have all been assigned attribute 'Fracture'. Other features and annotations can be added interactively. Borehole TB10.

iii. Labelling features

The common features in borehole TB10 and their geometric forms can, with aid of the accompanying OPTV imagery, be described by assigning combinations of the descriptive terms (attributes):

| | |
|---------------|---------------|
| Discontinuous | Open-fracture |
| | Fracture |
| | Quartz-vein |
| | Dark-vein |

A practical way of handling feature labelling is to have standard repertoires of attributes, available through 4 drop-down lists, under the general headings Type, Form, State and Remark. Additional attributes can be added to the lists for a particular borehole by the user.

In the manual and semi-automatic feature-picking modes, when sinusoids are calculated and displayed on the imagery 1 by 1, attributes can be assigned to features individually. In addition to the 4 drop-down lists of attributes, particular combinations of attributes that are used time and time again can be saved in a favourite features list, unique to that borehole.

3. Interpretation

The results of interactive depth-zonation of dips are shown as interpretation logs and a set of corresponding stereograms. In the case of Structural Interpretation dips assigned to bedding, lithological-banding, coal-seam or primary structures, are used. In the case of Fracture Analysis dips assigned to fractures or veins are used. Interpretation can be made using any combination of dips from Dipmeters, BHTV, OPTV and those measured directly on oriented cores, merged together by depth.

Dips can be filtered according to their attributes to produce multiple interpretations of the same borehole. In the case of borehole TB10 the BHTV dips were used. Since the borehole was drilled in granite, Structural Interpretation was not used. Two Fracture Analyses were made using:

1. All 343 dips (fractures, open-fractures, quartz-veins and dark-veins).
2. The 32 dips labelled as quartz-veins and dark-veins.

The 1st of these is described in detail in the following sections.

a. Fracture analysis

i. Identification of geometric sets.

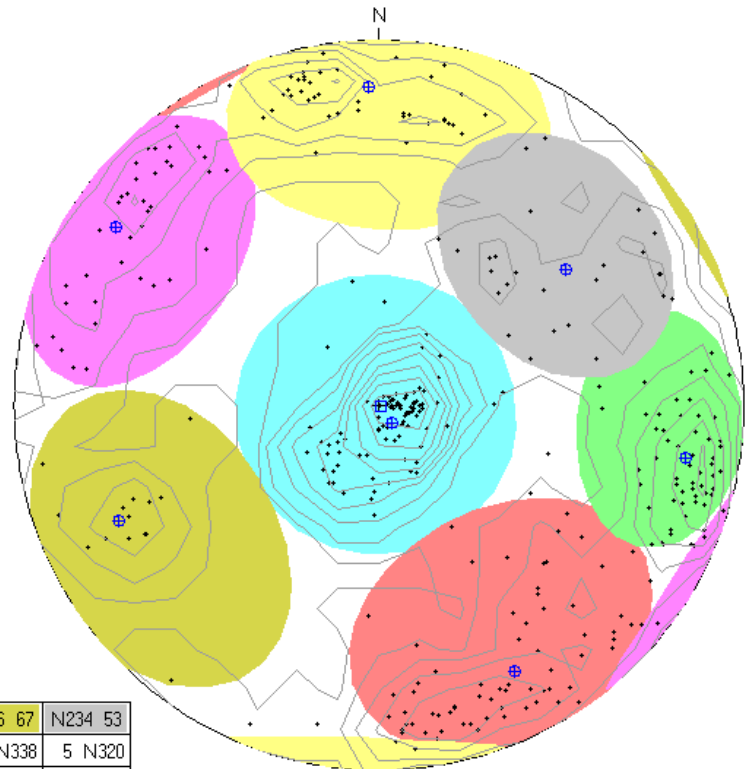
Poles to all 343 features for the whole log are shown on an equal-area, lower-hemisphere stereogram and contoured according to pole-density. Areas of high pole-density can be enclosed in up to 7 small-circles, drawn by trial and error on the stereogram. These are taken to define the natural geometric sets represented in the borehole. Mean-dips and mean-frequencies for the sets and lines of intersection among the sets are calculated and tabulated (Fig. 15). Mean dips, written as dip-azimuth and dip, for the fracture sets are used as labels, the small-circles are colour-coded. The labels and colour-coding persist throughout the depth-zonation procedure.

TB-10
 Zone 0, 13.000 - 61.000m
 Deviation 0.5 N134.7
 Mean dip format: dip-azimuth and dip
 dip data sets
 BHTV dips

| | mean dip | n | f |
|---------|----------|----|------|
| N322 5 | N322 5 | 93 | 1.96 |
| N333 71 | N333 71 | 67 | 4.15 |
| N280 74 | N280 74 | 54 | 4.05 |
| N124 76 | N124 76 | 42 | 3.74 |
| N178 76 | N178 76 | 43 | 3.76 |
| N066 67 | N066 67 | 14 | 0.74 |
| N234 53 | N234 53 | 23 | 0.80 |

intersections

| | N322 5 | N333 71 | N280 74 | N124 76 | N178 76 | N066 67 | N234 53 |
|---------|--------|---------|---------|---------|---------|---------|---------|
| N322 5 | | 1 N243 | 3 N009 | 2 N034 | 3 N267 | 5 N338 | 5 N320 |
| N333 71 | 1 N243 | | 70 N317 | 40 N046 | 36 N258 | 61 N025 | 48 N266 |
| N280 74 | 3 N009 | 70 N317 | | 38 N203 | 67 N232 | 39 N356 | 51 N210 |
| N124 76 | 2 N034 | 40 N046 | 38 N203 | | 74 N151 | 67 N070 | 47 N198 |
| N178 76 | 3 N267 | 36 N258 | 67 N232 | 74 N151 | | 59 N112 | 52 N249 |
| N066 67 | 5 N338 | 61 N025 | 39 N356 | 67 N070 | 59 N112 | | 10 N152 |
| N234 53 | 5 N320 | 48 N266 | 51 N210 | 47 N198 | 52 N249 | 10 N152 | |



equal-area lower-hemisphere 0-90
 contour-levels 1, 3, 6, 10, 15, 21, 28, 36, 45, □ well axis ⊕ mean dip

Fig. 15: Whole-well stereogram for all dips (fractures and veins) in borehole TB10.

ii. Depth zonation procedure.

Dips are shown on an arrow-plot, colour-coded according to geometric set. Histograms of frequency with depth, for each of the sets, are shown alongside the arrow-plot. These can be scrolled through the length of the complete log. Depth-zones are defined downwards, by selecting a series of depth-lines that separate different patterns of frequencies with depth. When a new depth-line is selected, poles to features for the new depth-zone are shown on a stereogram and mean-dips and frequencies for the sets are calculated and displayed. The depth-zone is then either accepted or rejected.

Apparent frequencies are calculated initially by counting the number of features in each set, over a certain measurement distance. These are converted to true frequencies using the cosine of the solid-angle between the pole to the mean-dip for the set and the borehole-axis. Since a minimum of 2 fractures is required to calculate an apparent frequency, there is a minimum-measurable true frequency that depends on measurement distance and the solid-angle. To reduce the effect of measurement distance on this minimum, the step distance between successive measurement stations is usually selected to be less than the measurement distance. The true frequencies are expressed as the number of features/metre, measured along the pole to the mean-dip of the set.

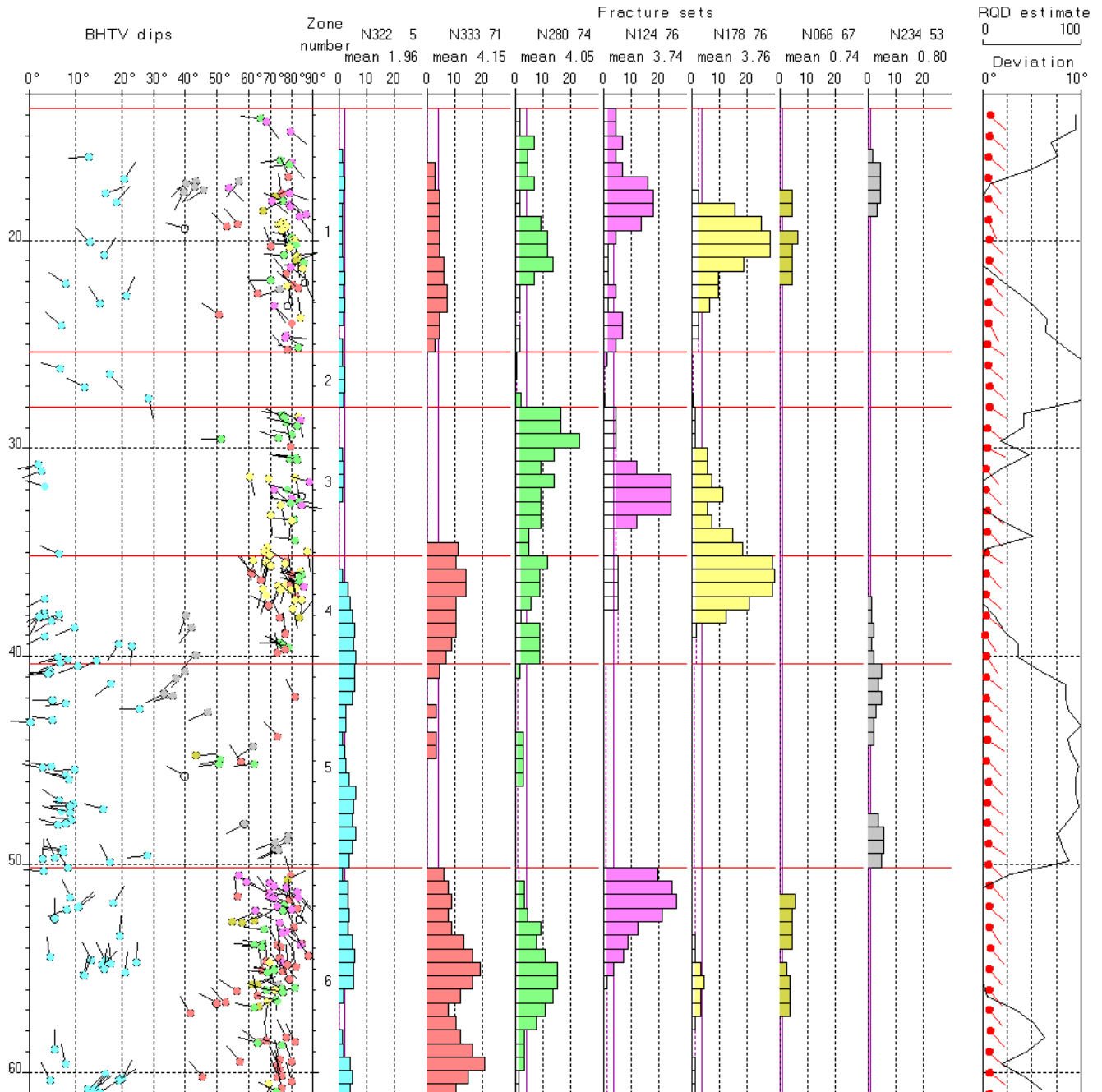


Fig. 16: Fracture Analysis log for all dips (fractures and veins) in borehole TB10.

iii. Log and stereograms.

In the case of borehole TB10 7 geometric sets of fractures and veins have been defined on the whole-well stereogram showing all 343 dips (Fig. 15), then divided into 6 depth-zones. The sub-horizontal N322° 5° (cyan) and steeper N333°

71° (red), N280° 74° (green), N124° 76° (pink) and N178° 76° (yellow) sets are dominant, both in terms of numbers and frequencies, the inclined N066° 67° (dirty yellow) and N234° 53° (grey) sets are less numerous and have mean-frequencies < 1/m. Out of the total 343 dips in the log, only 7 fall outside the defined fracture-sets, they are shown as open symbols on the arrow-plot.

In detail:

1. The sub-horizontal N322° 5° (cyan) set is ubiquitous, being represented in all depth-zones.
2. The steep N333° 71° (red) set is missing in zones 2 and 3 and only occurs with low frequencies in zone 5.
3. The steep N280° 74° (green) set is missing in zone 2 and only occurs with low frequencies in the middle of zone 5.
4. The steep N124° 76° (pink) set is missing in zones 2, 4, 5 and the lower part of zone 6.
5. The steep N178° 76° (yellow) set is missing in zones 2 and 5 and only occurs with low frequencies in the middle of zone 6.
6. The inclined N066° 67° (dirty yellow) set only occurs in middle parts of zone 1 and in zone 6.
7. The inclined N234° 53° (grey) set only occurs in middle parts of zone 1, lower parts of zone 4, upper and lower parts of zone 5.

The estimated Rock Quality Designation (RQD) log is superposed on the borehole deviation log in the final column of the log (Fig. 16). It is estimated from the Volumetric joint count (J_v), using the formula $RQD = 115 - 3.3J_v$, with $RQD = 100$ when $J_v < 4.5$ (Brown, 1981). J_v is calculated as the sum of the frequencies of the individual fracture sets, in each interval. RQD is very low in middle parts of zone 1, zones 3 and 4 and in upper parts of zone 6. It is very high in zones 2 and 5.

The 32 quartz- and dark-veins are restricted to:

1. The steep N333° 71° (red) set, where they are found in the upper part of zone 4 and zone 6.
2. The steep N280° 74° (green), only poorly represented.
3. The steep N178° 76° (yellow) sets, where they are found in zone 6 and locally attain frequencies of 12/m.

4. Discussion

Magnetic anomaly identification can be achieved by plotting the variation of the solid angle, G^H , between the earth's gravity and magnetic fields, with depth. Sonde orientation angles can be corrected once the anomalous zones are identified by interpolation of good values across the anomalous zones, or by importing a Gyro, Fotobor or Maxibor deviation survey. Where borehole deviation from the vertical exceeds a few degrees, anomalous image orientation can also be corrected. It is important that correct deviation data from upper parts of a log is used when calculating borehole trajectories. If not, because the calculation is a cumulative integration, the whole trajectory will be in error.

In deeper boreholes, in terrains of high stress, breakout phenomena may be identified and approximately characterized interactively on the travel-time/amplitude log. Once breakout zones are identified, more detailed characterization of breakout directions and apertures can be obtained by stacking up borehole cross-sections over selected parts of the log. Calculation of sonde decentralization is an integral part of this process and a reasonable estimate of borehole fluid velocity is necessary. If a caliper log is available a usable fluid velocity profile can be created from the travel-time log.

Dark vertical banding on the amplitude image, resulting from sonde decentralization, can be a nuisance when it obscures geologic detail. This can be corrected by using sonde decentralization estimates derived from the travel-time log. This greatly enhances the quality of the binary amplitude-gradients image, making both semi-automatic and automatic feature-picking more efficient.

Fully-automatic feature-picking works well on borehole image logs (BHTV and OPTV) for which a LoG-filtered, binary, gradients-image, showing white sinusoids without too much white background noise, can be produced. The time-consuming calculation of the Autofeats log can be done silently in the background, with no user-intervention.

Conversion of peaks on this log into meaningful sinusoids is a trial and error process. However, if time has been spent optimising the necessary filters for one borehole, the same filters can be used for logs from nearby boreholes in the same terrain. Interactive identification of small, undetected peaks, or elimination of spurious sinusoids is a simple, rapid process at this stage.

Many of the features that escape detection by fully-automatic processing, or are incorrectly processed, can be added or reprocessed in semi-automatic mode. Dips resulting from fully-automatic or semi-automatic processing are totally objective, being derived exclusively from information contained in the image. Finally, manual feature-picking mode can be selected to finish processing those features that can not be done in semi-automatic mode.

Production of meaningful interpretations is greatly enhanced by the ability to select features according to their attributes. The more care that is taken with assignment of these attributes, the greater the interpretation possibilities.

5. Acknowledgments

Our thanks to SEKOGEO Co. Ltd. for permission to use the TB10 log as an example in this discussion.

The automatic and semi-automatic feature-picking methods described here are based extensively on development work carried out by former colleague Dr. Kevin Glossop and scientific collaboration with Prof. Paul Lisboa (Liverpool, John Moores Univ.) and Dr. Paul Russell (Univ. of Liverpool) under a Teaching Company Scheme (TCS). This is gratefully acknowledged.

6. References

E.T. Brown. Rock Characterization, Testing and Monitoring. *ISRM Suggested Methods*, Pergamon Press 1981, 211p.

K.J. Glossop, A.W.B. Siddans, P.J.G. Lisboa and P.C. Russell. Robust and efficient PC based software for the semi automatic interpretation of borehole televiewer data. In *SEG Int. Exp. & 67th Annual Meeting*, Nov. 2-7, Dallas 1997, 2046-2049.

K.J. Glossop, P.J.G. Lisboa, P.C. Russell, A.W.B. Siddans and G.R. Jones. An implementation of the Hough Transformation for the Identification and Labelling of Fixed Period Sinusoidal Curves. *Computer Vision and Image Understanding*. 74(1), 1999, 96-100.

A.W.B. Siddans. Structural geology using borehole wall imagery: case study of an OPTV log in flagstones, North Scotland. *First Break*. 20, 2002, 623-629.

Zemanek, J., Beam Behaviour within the Nearfield of a Vibrating Piston. *J. Acoust. Soc. Amer.*, 49(1), 1971, p.181-191.

Appendix I - Acoustic televiewer beam geometry

Using the coordinate system shown in Fig I:

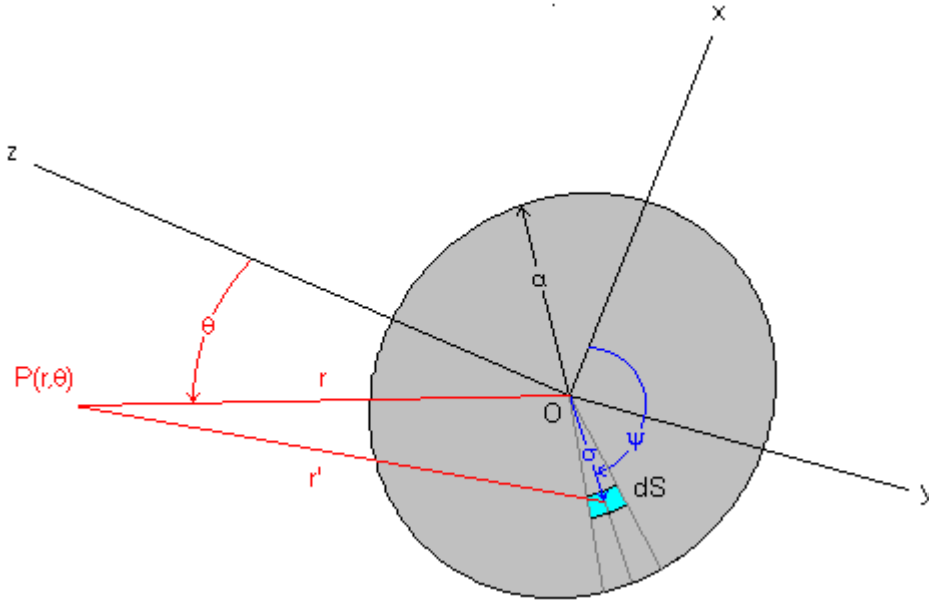


Fig.I: Coordinate system and parameters used in the calculation of acoustic beam pressure. The transducer surface lies in the xy-plane, 0z is the transducer axis.

Zemanek (1971) notes that the pressure at any point P(r,θ) in the acoustic beam in front of a flat, circular transducer is the total contribution from incremental areas, dS, of the transducer surface. This total pressure is given by:

$$p = \frac{j\rho ck}{2\pi} U_0 \int_0^a \sigma d\sigma \int_0^{2\pi} \frac{e^{j(\omega t - kr')}}{r'} d\psi \quad \text{Eq. 1}$$

$$j = \sqrt{-1}$$

ρ = medium density

c = medium velocity of sound

wavenumber $k = 2\pi/\lambda$

λ = wavelength of sound

$\omega t = 2\pi \times \text{frequency} \times \text{time}$

U_0 = peak amplitude of transducer velocity

r = distance from point P to center of transducer

r' = distance from point P to incremental area dS

$$r' = (r^2 + \sigma^2 - 2r\sigma \sin \theta \cos \psi)^{1/2} \quad \text{Eq. 2}$$

When the expression for distance r' (Eq. 2) is substituted into Eq. 1, the resulting expression is so complicated that a closed-form solution cannot be obtained.

The pressure distribution in an acoustic beam ahead of a circular transducer has axial symmetry. Relative pressure P, at points (z,x) in the zx-plane is calculated as a double summation of contributions from elemental areas of the transducer using:

$$P(Z, X) = \left| \sum_{p=1}^m \sum_{q=1}^n \frac{\Delta S_q}{R_{pq}} e^{j\left(\frac{a}{\lambda}\right)^2 R_{pq}} \right| \quad \text{Eq. 3}$$

elemental area $\Delta S_q = \sigma_q \Delta \sigma \Delta \psi$

$$\sigma_q = \Delta \sigma (q - 0.5)$$

$$\Delta \sigma = \frac{1}{na/\lambda} \quad \Delta \psi = \pi/m$$

$$n = 4a/\lambda \quad m = n\pi$$

$$R_{pq} = (R^2 + \sigma_q^2 - 2R\sigma_q \sin \theta \cos \psi)^{1/2}$$

$$R = (Z^2 + X^2)^{1/2}$$

$$\theta = \tan^{-1}(X/Z)$$

$$\psi_p = \Delta\psi(p - 0.5)$$

Variables Z and X are dimensionless and defined as $Z = \frac{z}{a^2/\lambda}$ $X = \frac{x}{a^2/\lambda}$

The pressure plots produced here extend from 0 thru 1.5a in the X-direction (radially outwards from the center of the transducer surface), from 0 thru Z=4 in the Z-direction (away from the center of the transducer surface along the transducer axis). Transducer frequency 1.5MHz is used throughout. The computational grid used has 48 points in the X-direction, 400 points in the Z-direction.

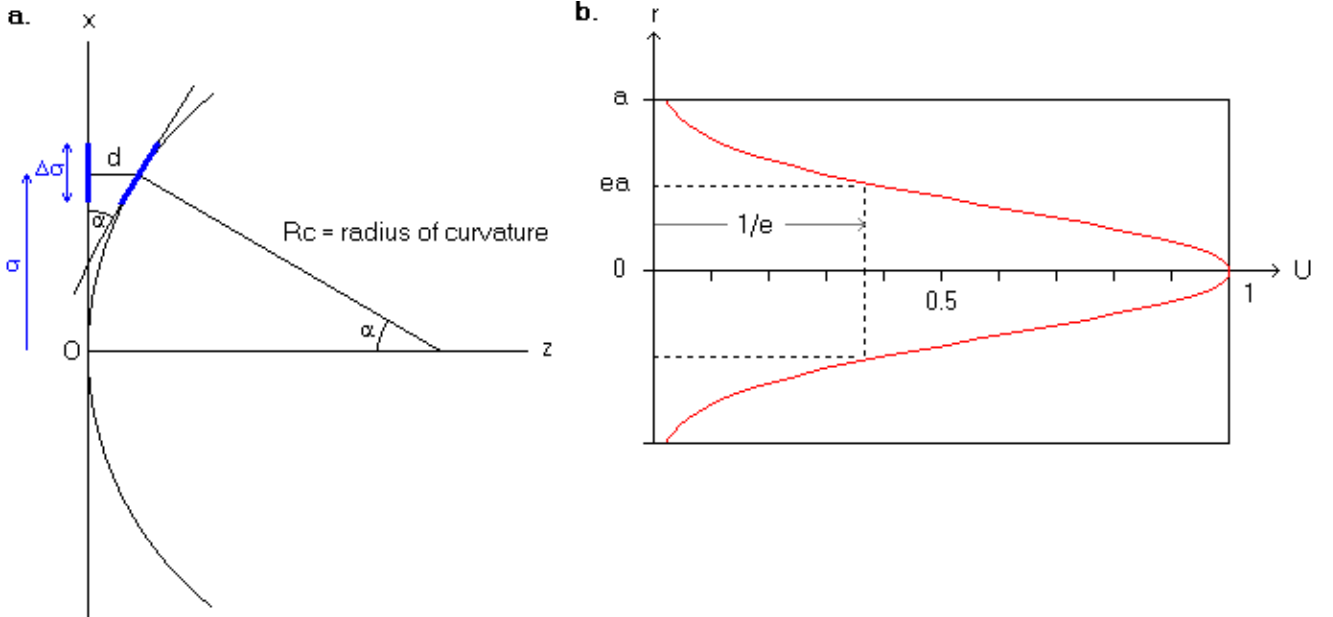


Fig. II: a. Concave transducer geometry, b. peak amplitude distribution on the surface of a 'Gaussian' transducer.

In the case of concave transducers (Fig. IIa), additional terms enter Eq. 2, defining the distance r' between points $P(r,\theta)$ and the center of elemental areas dS :

$$r' = [r^2 + \sigma^2 - 2r(\sigma \sin \theta \cos \psi - d \cos \psi) + d^2]^{1/2} \quad \text{Eq. 2a}$$

$$d = Rc(1 - \cos \alpha)$$

$$\alpha = \sin^{-1}\left(\frac{\sigma}{Rc}\right)$$

A Gaussian distribution of peak amplitude of transducer surface velocity is characterized by the effective radius, ea (Fig. IIb). At any radial distance r away from the center of the transducer, peak amplitude of transducer surface velocity U_r is given by:

$$U_r = U_0 \exp\left(-\frac{r^2}{ea^2}\right) \quad \text{Eq. 4}$$

Where U_0 is the maximum peak amplitude of transducer surface velocity at the transducer center. This is implemented in the calculation of pressure distribution, using Eq. 3, by assigning a similar pressure distribution to elemental areas ΔS_q , according to radial distance σ_q .

Calculated relative pressure and pressure-drop distributions results obtained for transducers with a/λ ratios = 2.5 and 5.0 reproduce those reported by Zenamek (1971, Figs. 5,6,8,9,11,12), even in the complex nearfield. Equivalent distributions for the HiRAT transducer configuration ($a/\lambda = 9.5$) are shown in Figs. III-VI.

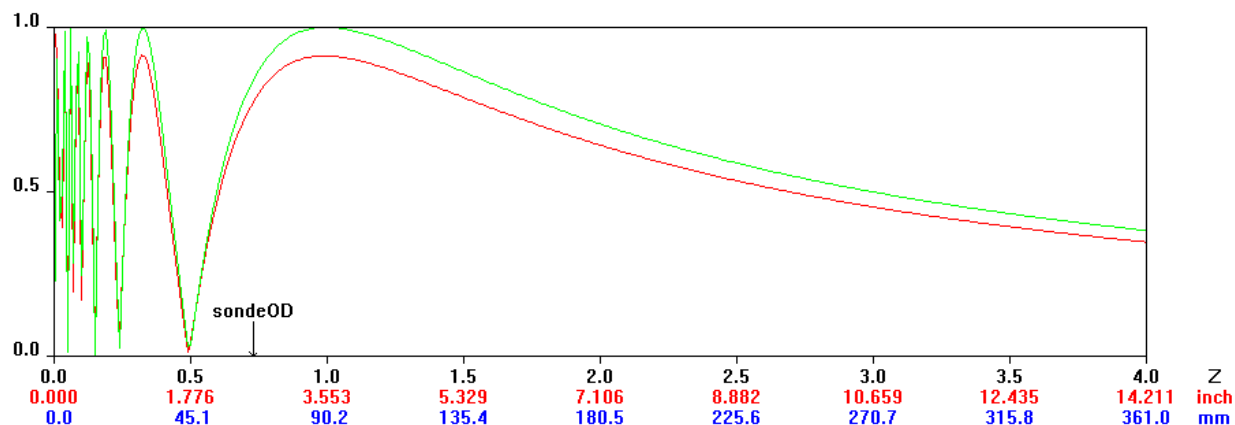


Fig. III: On-axis relative pressure distribution, calculated directly using Eq. 5 (green), by summation Eq. 3 (red).

The on-axis relative pressure distribution can be calculated directly, using a solution to Eq. 1 with $\theta=0$ in Eq. 2:

$$p = \sin \left[\frac{k \cdot z}{2} \left(\sqrt{1 + \left(\frac{a}{z} \right)^2} - 1 \right) \right] \quad \text{Eq. 5}$$

Fig. III (red trace) shows the on-axis pressure calculated by summation of contributions from all elemental areas of the transducer surface, i.e. the full implementation of Eq. 3. The results of this simpler calculation are shown as the green trace. Ideally the two traces should be identical. The differences between them represent the inaccuracies that result from using a finite number of elemental areas of finite size, rather than an infinite number of infinitesimally small elemental areas.

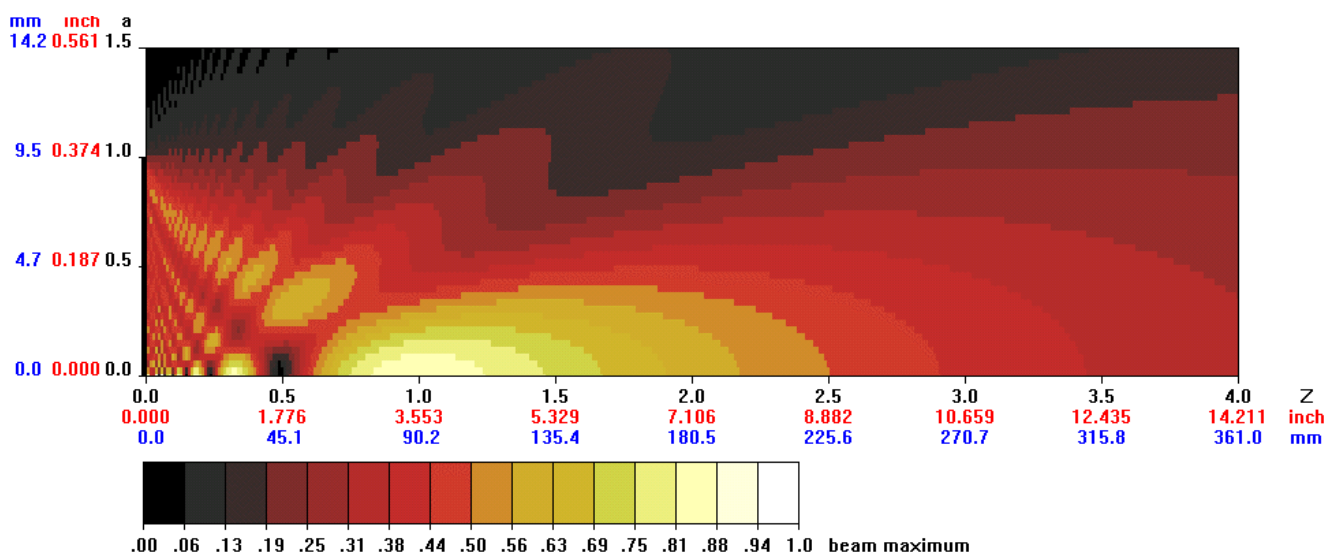


Fig. IV: Relative pressure distribution.

Note that distance along the Z-axis starts with $z=0$ at the transducer surface. Distance from here to the 45° rotating mirror of the HiRAT sonde is 45mm, then the mirror-center to external surface of the sonde distance (without centralizers) is a further 22.5mm.

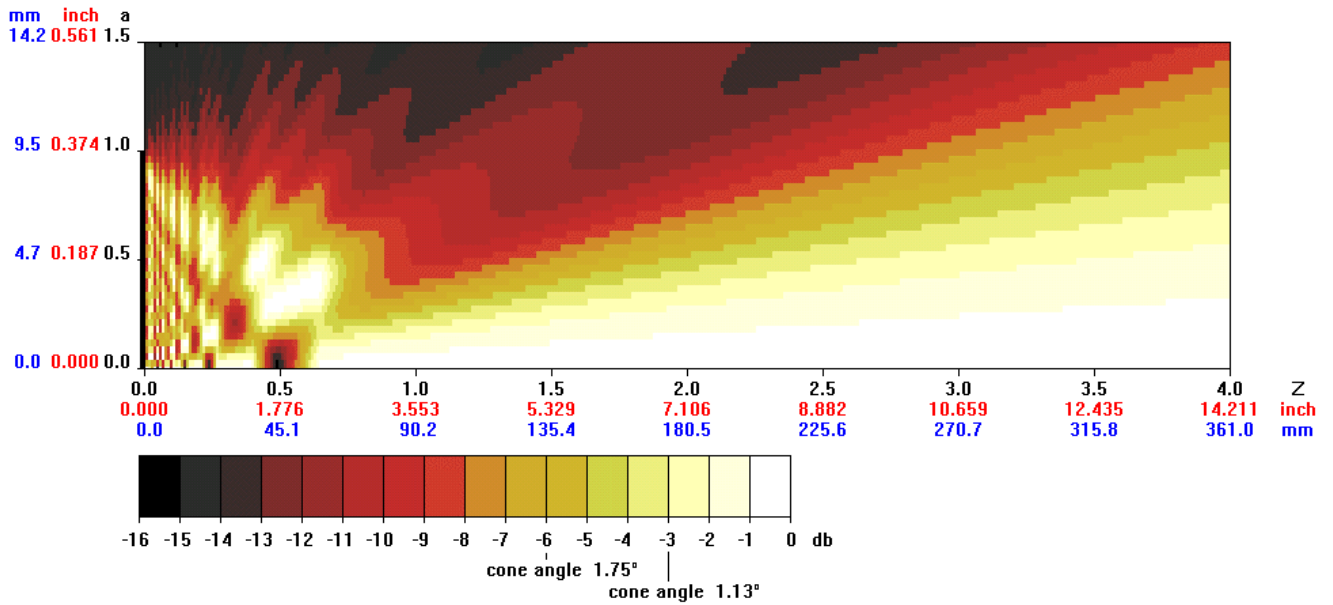


Fig. V: Relative pressure drop (dB).

The cone angle defined by the -3dB pressure drop contour is often used to define beam width. For the HiRAT sonde discussed here it is 1.13°. Details of the complex pressure distribution in the nearfield are shown as a surface in Fig. VI.

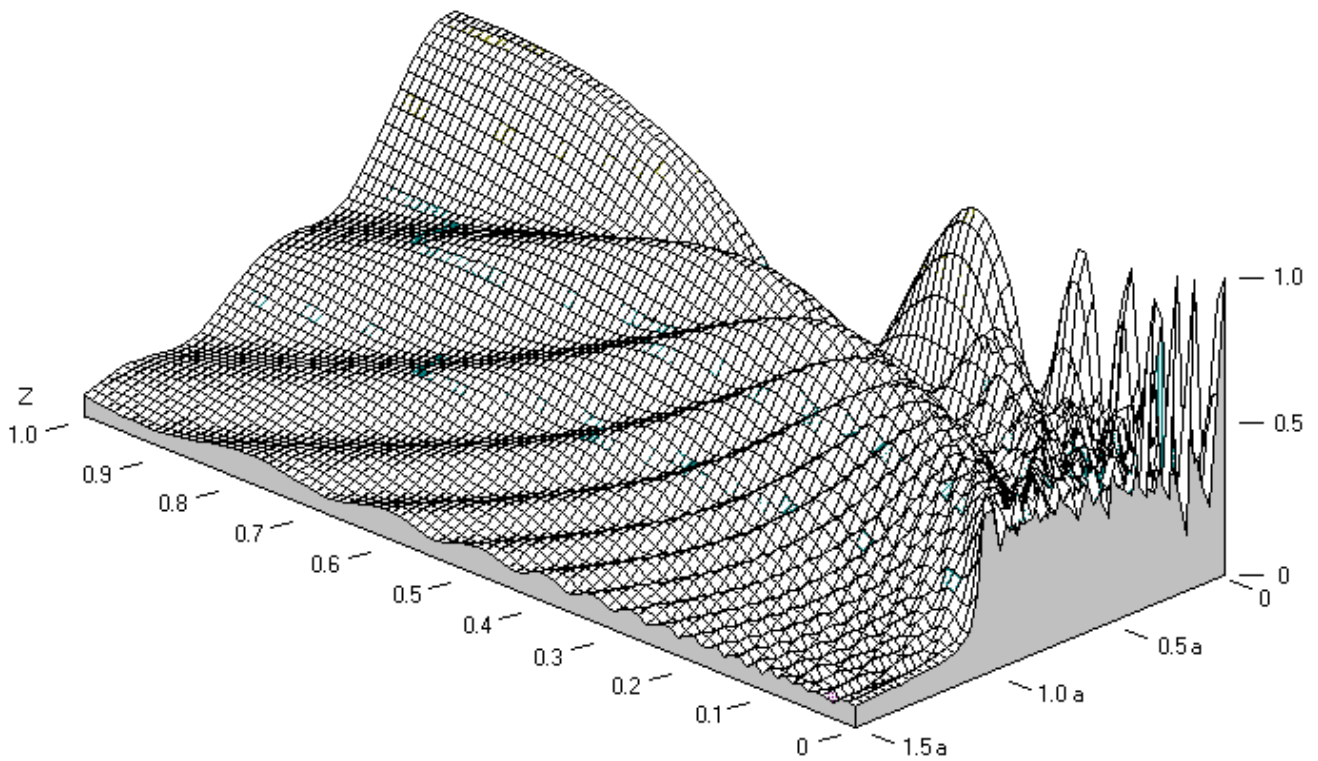


Fig. VI: Acoustic pressure within the nearfield shown as a surface.

From the sonde's point of view, as seen from the sonde-axis, point P has azimuth $\theta' = \beta + \lambda$. From the borehole's point of view, as seen from the borehole-axis, point P has azimuth $\theta = \beta + \gamma$. The only material points on the trace of the intersection of the oblique plane with the borehole-wall, with the same azimuth viewed from both Q and Q', occur in directions $\theta = \theta' = \beta$ and $\theta = \theta' = \beta + \pi$. In general there is an azimuth difference $\mu = \theta' - \theta = \lambda - \gamma$.

In $\Delta QPQ'$, $R \cdot \sin(\lambda - \gamma) = t \cdot \sin(\pi - \lambda) = t \cdot \sin \lambda$, which leads to:

$$\gamma = \lambda - \sin^{-1}\left(\frac{t \cdot \sin \lambda}{R}\right) \quad \text{Eq. 6}$$

$$\lambda = \tan^{-1}\left(\frac{R \cdot \sin \gamma}{R \cdot \cos \gamma - t}\right) \quad \text{Eq. 7}$$

$$\mu = \sin^{-1}\left(\frac{t \cdot \sin \lambda}{R}\right) \quad \text{Eq. 8}$$

In borehole-axes QEN, point Q' has coordinates $[t \cdot \sin \beta, t \cdot \cos \beta]$, point P $[R \cdot \sin(\beta + \gamma), R \cdot \cos(\beta + \gamma)]$, which leads to:

$$v = \left(t^2 - 2tR \cos \gamma + R^2\right)^{1/2} \quad \text{Eq. 9}$$

$$v=R \text{ in directions } \gamma = \cos^{-1}\left(\frac{t}{2R}\right) \quad \text{Eq. 10}$$

A short section of a decentralized HiRAT amplitude/travel-time log, borehole radius $R=38\text{mm}$, decentralization $t=8\text{mm}$, $\beta=131^\circ$, is shown in Fig. IX (upper).

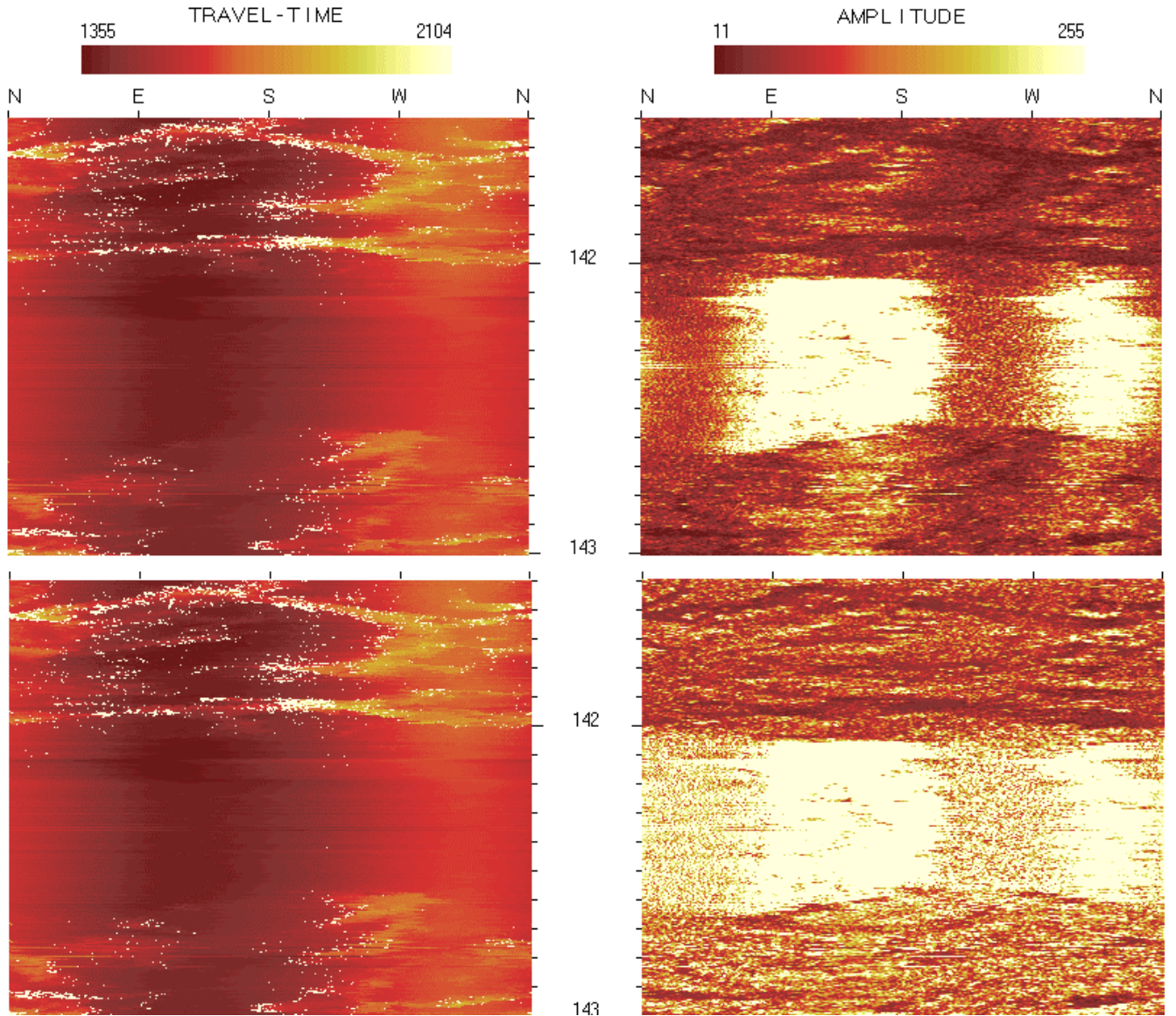


Fig. IX: Section of HiRAT log before (upper) and after (lower) correction for sonde decentralization, $R=38\text{mm}$, $t=8\text{mm}$, $\beta=131^\circ$. Borehole deviation from vertical = 40° , deviation azimuth N301°.

The high-side of a borehole is in the direction of deviation azimuth, the low-side is at $+180^\circ$, the weight of the sonde has flattened its bow-spring centralizers on the low-side. The distribution of amplitude image brightness around the borehole-wall, at 142.499m depth, is shown in Fig. X. This is calculated at 1° intervals, as the mean value over a $(1+2m) \times (1+2n)$ block of pixels in the rasterized image, where m is the number of neighbors vertically, n horizontally, expressed as a percentage of maximum brightness at that depth.

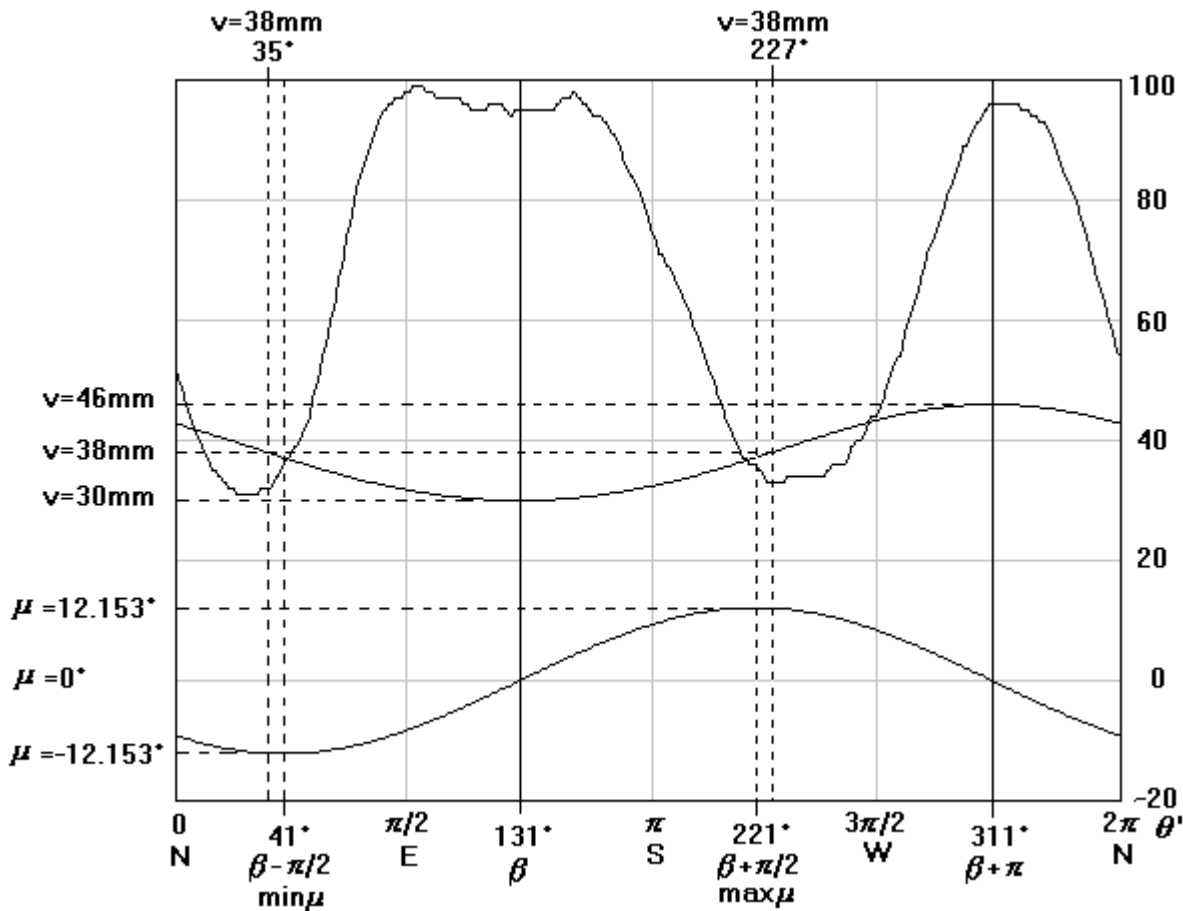


Fig. X: Curves showing variations in image brightness (upper), mirror-center to borehole-wall distance (v) and beam incidence angles at the borehole-wall (μ , 0 =perpendicular), with azimuth θ' , as seen from the sonde-axis. Parameters $m=n=9$ were used to calculate the image brightness curve.

The brightness distribution is periodic, but the maximum in the SE sector is wider than that in the NW sector. Similarly, the minimum in the SW sector is wider than that in the NE sector.

Also shown in Fig. X are variations in mirror-center to borehole-wall distance (v) and beam incidence angle on the borehole-wall (μ), with variation in azimuth (θ') as seen from the sonde-axis. Note that:

1. Mirror-center to borehole-wall distance (v) has minimum value, $R-t = 30$ mm, in the sonde decentralization direction β , maximum value, $R+t = 46$ mm, in the opposite direction $\beta+\pi$. $v=R=38$ mm in directions 35° and 227° , which are displaced from the $\beta-\pi/2$ and $\beta+\pi/2$ directions by -6° and $+6^\circ$ respectively.
2. Beam incidence angle on the borehole-wall (μ , $\mu=0$ when the beam is perpendicular) has a minimum value -12.153° in direction $\beta-\pi/2$, maximum value 12.153° in direction $\beta+\pi/2$. It is 0 in directions β and $\beta+\pi$.
3. Minima on the image brightness curve are displaced from the $\beta-\pi/2$ and $\beta+\pi/2$ directions, in the same sense as the $v=R$ directions, but even more so.

These variations arise simply from the geometry of sonde decentralization and are likely to contribute to the observed distribution of image brightness.

Curves showing the variation of v and μ with θ , from the borehole-axis viewpoint, are shown in Fig. XI.

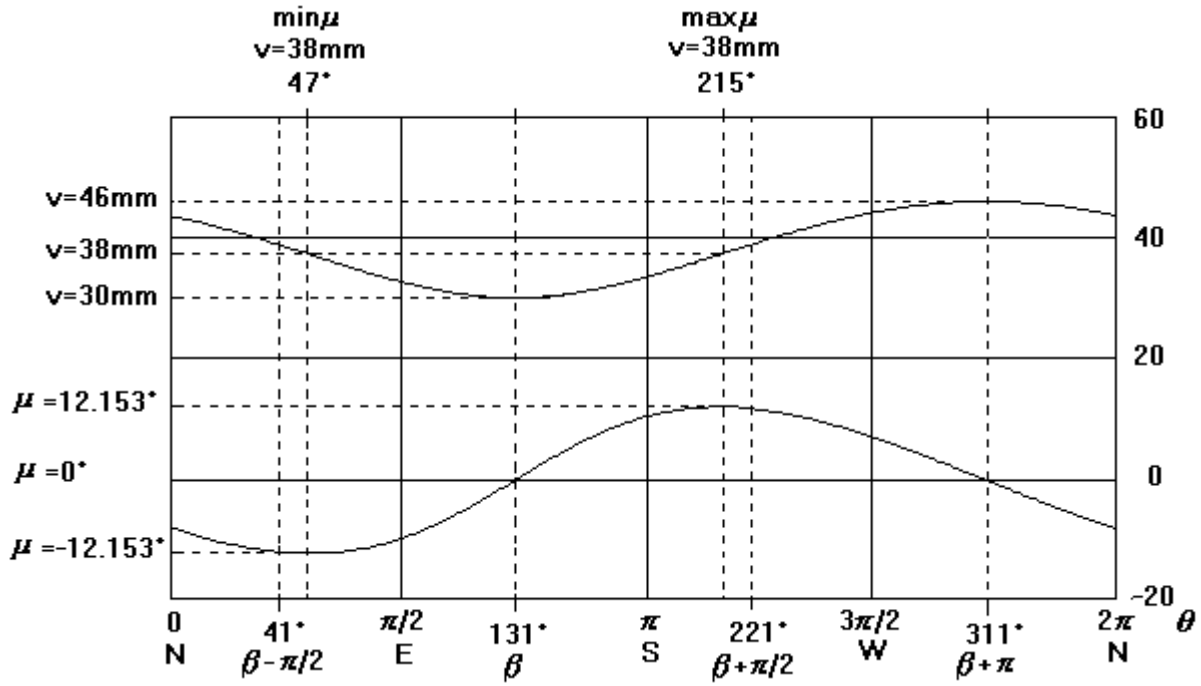


Fig. XI: Curves showing variations in mirror-center to borehole-wall distance (v) and beam incidence angles at the borehole-wall (μ , 0 =perpendicular), with azimuth θ , as seen from the borehole-axis.

1. As in Fig. X, mirror-center to borehole-wall distance (v) has minimum value, $R-t = 30\text{mm}$, in the sonde decentralization direction β , maximum value, $R+t = 46\text{mm}$, in the opposite direction $\beta+\pi$. However, $v=R=38\text{mm}$ in directions 47° and 215° , which are here displaced from the $\beta-\pi/2$ and $\beta+\pi/2$ directions by $+6^\circ$ and -6° respectively (Eq. 10).
2. Beam incidence angle on the borehole-wall (μ , $\mu=0$ when the beam is perpendicular) here has a minimum value -12.153° in direction $\beta-\pi/2+6^\circ$, maximum value 12.153° in direction $\beta+\pi/2-6^\circ$. It is 0 in directions β and $\beta+\pi$.

Variations of relative pressure on the beam-axis at the borehole-wall and on return to the transducer and beam width at the -3dB pressure drop contour, with azimuth θ' , as seen from the sonde-axis, are shown in Fig. XII.



Fig. XII: Variation in a. Relative pressure on the beam-axis at the borehole-wall (solid line) and on return to the transducer (broken line), b. Beam width at the -3dB pressure drop contour, with azimuth θ' as seen from the sonde-axis.

Variation in relative pressure on the beam-axis was calculated using transducer to mirror-center distance + the mirror-center to borehole-wall distance data (v in Fig. X). No account is taken of pressure drops at reflections off the mirror and borehole-wall, values are taken from the corresponding distances in Fig. III (Appendix I). Note:

1. Minimum pressure at the borehole-wall is in the direction of decentralization β , maximum pressure in the $\beta+\pi$ direction. This is because the corresponding distances, 75mm and 91mm, are located at points before and at the major beam-pressure maximum at $Z=1$ (see Fig. III, Appendix I). On return to the transducer, after reflection off the borehole-wall, both corresponding distances, 150mm and 182mm, are located beyond this maximum and the situation is reversed, with maximum pressure in direction β .
2. The -3dB pressure-drop contour, often used to define beam width, has a cone-angle of 1.13° (see Fig. V, Appendix I). Beam width is a linear function of the transducer to mirror-center + mirror-center to borehole-wall distance, so has minimum value in the direction of decentralization β and maximum value in direction $\beta+\pi$.

The wide brightness maximum in the decentralization direction β , compared with that in direction $\beta+\pi$ (Fig. X), is seen in other decentralized logs produced by the acoustic sonde. Slim boreholes seem to be more subject to this than larger boreholes and width difference appears to increase with increasing decentralization. Another phenomena, not particularly well illustrated in Fig. X, is that the values of the two brightness minima can be significantly different. All of which indicates that no simple correction for variable image brightness with azimuth can be universally applied. The following, empirical correction technique has been used with some success.

Two different sinusoids are calculated for the two sectors on the brightness v azimuth (θ') curve that intervene below the two maxima. These can have different mean-values, phase-shift and amplitude. The trick is to correctly determine the azimuth ranges used to calculate them and then apply the resulting correction. The procedure is illustrated in Fig. 6.

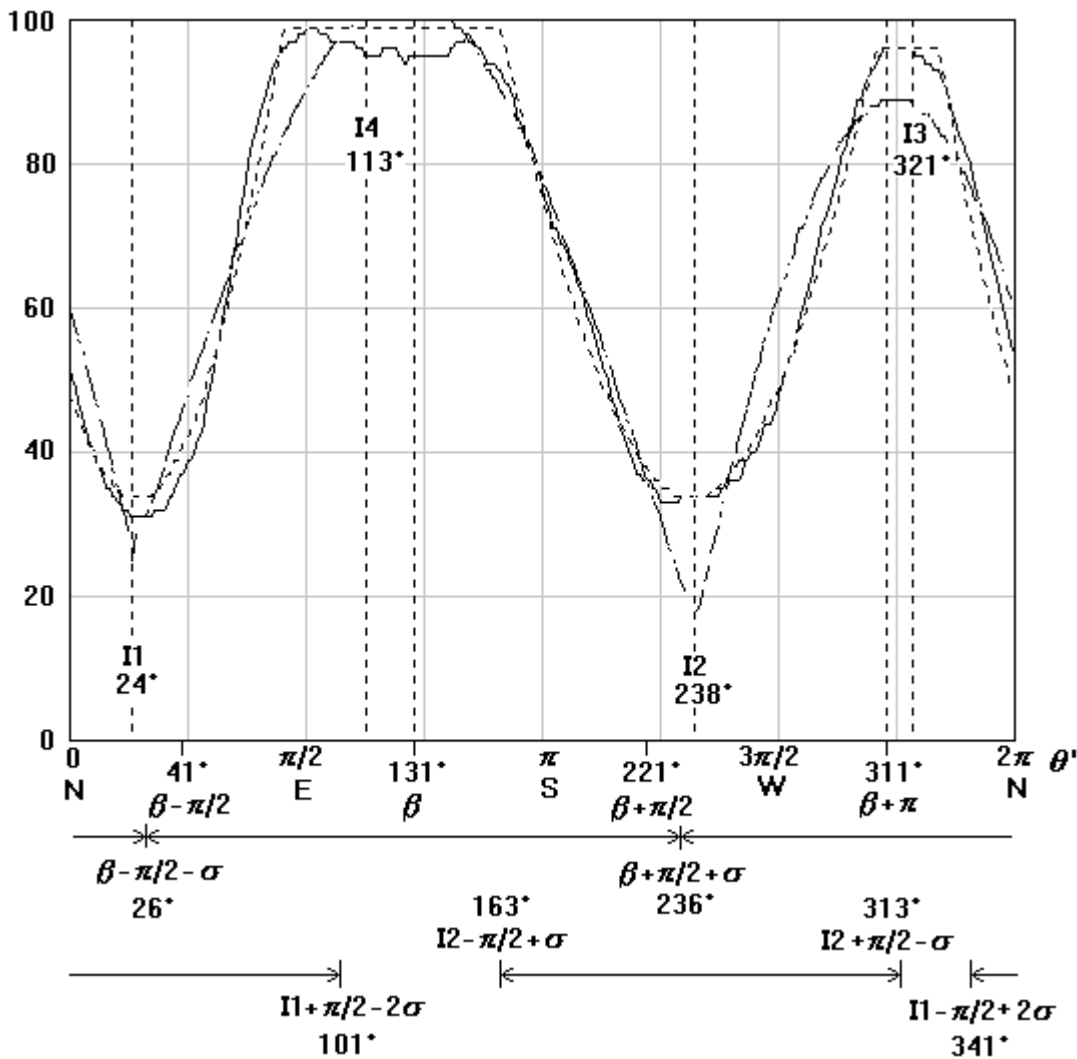


Fig. XIII: Brightness correction in a borehole with radius $R=38\text{mm}$ and sonde decentralization $t=8\text{mm}$ in direction $\beta=131^\circ$. The same brightness profile (solid line) is used as in Fig. X.

Step 1. A search range angle is calculated, $\sigma = 10^*(R+t)/(R-t)$, where t = decentralization-distance and R = borehole radius. This is used to define 2 azimuth ranges, extending from $(\beta-\pi/2-\sigma)$ thru $(\beta+\pi/2+\sigma)$ and $(\beta+\pi/2+\sigma)$ thru $(\beta-\pi/2-\sigma)$, where β = decentralization direction. A 1st set of sin curves (dashed lines in Fig. 6) is calculated from brightness values (solid line in Fig. 6) within these azimuth ranges. These intercept each other at azimuths I1 and I2, approximately at mid-points in the 2 brightness maxima.

Step 2. New azimuth ranges are defined, extending from $(I1-\pi/2+2\sigma)$ thru $(I1+\pi/2-2\sigma)$ and $(I2-\pi/2+\sigma)$ thru $(I2+\pi/2-\sigma)$. A 2nd set of sin curves (dotted lines in Fig. 6) is calculated from brightness values within these azimuth ranges. These intercept each other at azimuths I3 and I4, approximately at mid-points in the 2 brightness minima.

Step 3. Local brightness maxima are found within azimuth ranges $(I1-\pi/2)$ thru $(I1+\pi/2)$ and $(I2-\pi/2)$ thru $(I2+\pi/2)$, the 2nd set of sin curves are truncated to the local maxima values where they exceed them.

The truncated, 2nd set of sin curves are used to correct the current line in the amplitude image for brightness loss due to decentralization. The process is repeated for all lines in the amplitude image. Local contrast in the amplitude imagery is preserved because brightness curves for each image line are calculated over a block of $(1+2m) \times (1+2n)$ pixels, centered on the current pixel in the current line. The original amplitude image seen in Fig. IX (upper), is improved to that shown in Fig. IX (lower) after correction. The travel-time image is left unchanged.

Appendix III - Dip calculation and decentralized sondes

Traditional, manual feature-picking on borehole-wall imagery, in which a series of points are digitised on feature traces, is illustrated in Fig. XIV.

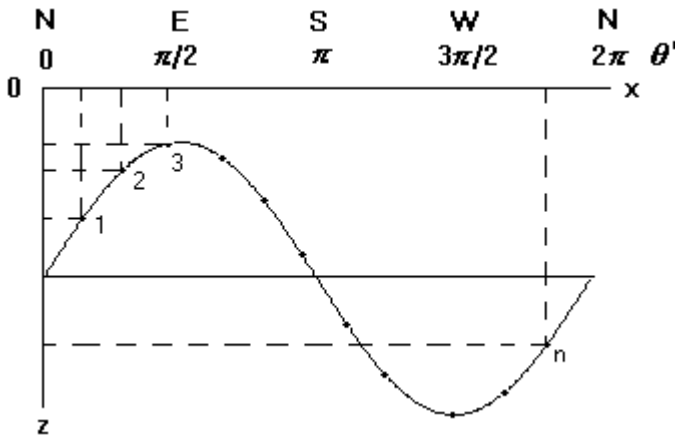


Fig. XIV: Series of data points $(x_1, z_1), (x_2, z_2), \dots, (x_n, z_n)$ digitised on a feature trace.

The individual coordinates are entered in data point arrays, $X = (x_1, x_2, \dots, x_n)$ and $Z = (z_1, z_2, \dots, z_n)$, converting x-values to azimuths (θ' as seen from the sonde-axis) and z-values to depths. An array of corresponding radii values, $R = (r_1, r_2, \dots, r_n)$, is also set up. Individual values can be set to a nominal borehole radius, or in the case of acoustic imagery with good quality travel-time data and an estimate of acoustic velocity in the borehole-fluid, they can be calculated from travel-time values.

A 1st estimate of feature depth is given by $d_o = \frac{\sum z_i}{n}$, ($i = 1, n$) Eq. 11

$$c_{i,1} = r_i \cdot \cos(\theta'_i)$$

The data arrays can be entered into a data matrix $C(n,3)$, where $c_{i,2} = r_i \cdot \sin(\theta'_i)$, ($i = 1, n$) Eq.12

$$c_{i,3} = z_i - d_o$$

It is convenient to calculate mean radius in this loop, $rc = \exp\left[\frac{\sum \ln(r_i)}{n}\right]$ Eq. 13

A linear equation system, with coefficients $A(3,3)$ and $B(3)$, can now be set up:

$$\begin{aligned} a_{1,1} &= n & a_{1,2} &= \sum c_{i,1} & a_{1,3} &= \sum c_{i,2} & b_1 &= \sum c_{i,3} \\ a_{2,1} &= \sum c_{i,1} & a_{2,2} &= \sum (c_{i,1})^2 & a_{2,3} &= \sum c_{i,1} \cdot c_{i,2} & b_2 &= \sum c_{i,1} \cdot c_{i,3} \\ a_{3,1} &= \sum c_{i,2} & a_{3,2} &= \sum c_{i,2} \cdot c_{i,1} & a_{3,3} &= \sum (c_{i,2})^2 & b_3 &= \sum c_{i,2} \cdot c_{i,3} \end{aligned} \quad (i = 1, n) \quad \text{Eq.14}$$

Solve this to get $AA(3,3)$ and $BB(3)$, which gives 2nd estimate of feature depth $d_o += bb_1$, then recalculate $c_{i,3} = z_i - d_o$.

Sum products for moments of inertia about axes and products of inertia $M(3,3)$:

$$\begin{aligned}
m_{1,1} &= \sum (c_{i,2}^2 + c_{i,3}^2) & m_{1,2} &= -\sum c_{i,1} \cdot c_{i,2} & m_{1,3} &= -\sum c_{i,1} \cdot c_{i,3} \\
m_{2,1} &= -\sum c_{i,1} \cdot c_{i,2} & m_{2,2} &= \sum (c_{i,3}^2 + c_{i,1}^2) & m_{2,3} &= -\sum c_{i,2} \cdot c_{i,3} \\
m_{3,1} &= -\sum c_{i,1} \cdot c_{i,3} & m_{3,2} &= -\sum c_{i,2} \cdot c_{i,3} & m_{3,3} &= \sum (c_{i,1}^2 + c_{i,2}^2)
\end{aligned} \quad (i = 1, n) \quad \text{Eq. 15}$$

M is the matrix representation of the 2nd order Moment of Inertia tensor, it follows the transformation of axes law $\mathbf{B}=\mathbf{R}\mathbf{A}\mathbf{R}^T$ and can be diagonalized to obtain the eigenvalues and eigenvectors. The 3rd eigenvector contains the direction cosines DC(3) of the pole to the best-fit plane through the digitised points. The resulting dip azimuth is correct.

$$\text{Calculate error measure } p_o = 100 \cdot \frac{\sum |c_{i,1} \cdot dc_1 + c_{i,2} \cdot dc_2 + c_{i,3} \cdot dc_3|}{n \cdot rc}, \quad (i = 1, n) \quad \text{Eq. 16}$$

p_o is the mean perpendicular misfit of points from the calculated plane, expressed as a percentage of mean borehole radius. It is independent of dip and borehole diameter.

If travel-time has been used and sonde decentralization calculated, a 3rd estimate of depth can be made:

$$d_o + = t \cdot \tan \delta \quad \text{Eq.17}$$

where t = decentralization distance, δ = calculated dip. This gives depth on the borehole-axis, the earlier estimates were depth on the sonde-axis.

The geometry of decentralized sondes is discussed in Appendix II. Fig. XV shows the unrolled traces of planes dipping at 50° and with dip azimuths N070°, N160°, N250° and N340°, viewed from both the borehole-axis and sonde-axis, with the sonde decentralized 8mm in direction $\beta=131^\circ$, in a 38mm diameter borehole.

1. The solid and broken traces intersect each other in directions β and $\beta+\pi$.
2. The broken traces (borehole-axis view) have their low points in dip azimuth directions and their high points at +180°, the solid traces (sonde-axis view) do not.
3. The azimuth difference between points at the same depth on the solid (sonde-axis view) and broken traces (borehole-axis view) is distributed according values of angle μ (see Appendix II, Fig. XI and Eq. 8).
4. The broken traces (borehole-axis view) are sinusoidal, the solid traces (sonde-axis view) are not quite sinusoidal.

The procedure outlined above calculates dip azimuths and dips correctly in decentralized image logs, but unless the 3rd estimate of depth is made, using decentralization-distance and dip magnitude (Appendix II, Eq. 17), the estimated feature depth will be that on the sonde-axis rather than that on the borehole-axis.

Dip calculation methods that rely on feature traces being sinusoidal, including the semi-automatic and automatic methods described by Glossop *et al.* (1999) and Siddans (2002), will work less well in decentralized image logs. In particular:

1. Dip azimuth estimates based on identifying the low point of feature traces will be wrong by an amount depending on borehole radius, R , decentralization distance, t and azimuth β , dip azimuth, α and magnitude δ . In the examples shown in Fig. 8 the errors range up to 12°.
2. Dip azimuth estimates based on strike direction calculation as $\omega' = (\theta'_{max} + \theta'_{min})/2$, will work better, providing care is taken in digitizing the θ'_{max} and θ'_{min} directions. Strike direction is the azimuth of a horizontal line drawn in an inclined plane, $\omega = (\alpha - \pi/2)$ or $(\alpha + \pi/2)$, where α is dip azimuth. In the examples shown in Fig. 8 the errors only range up to 1.5°.
3. Dip magnitude estimates based on the difference in feature depths in the θ'_{max} and θ'_{min} directions, depend on how well borehole radius, R , is estimated.
4. Flexible sinusoid methods, in which a sinusoidal shape is interactively adjusted to superpose a feature trace, are like (2), providing care is taken to balance the misfits at the high and low points equally.
5. Semi-automatic and automatic methods are also like (2) and will automatically balance the misfits at the high and low points equally, providing enough of the pixels defining the feature trace are close enough to a sinusoid to form a bright spot in Hough space, so that the feature is identified.

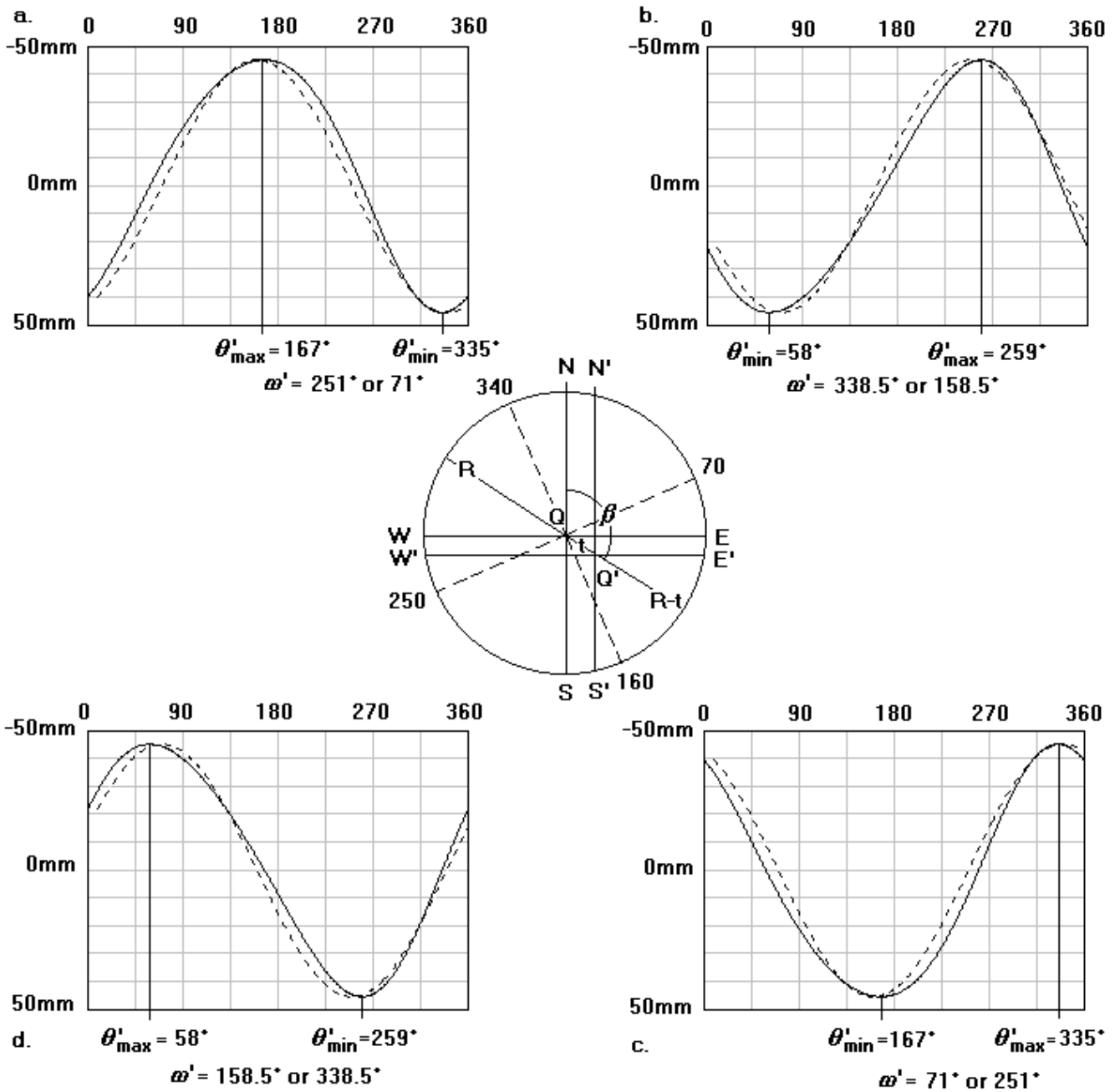


Fig. XV: Unrolled traces of planes dipping at 50° , with dip azimuth a. N340°, b. N070°, c. N160°, d. N250°, in a 38mm diameter borehole, with sonde decentralized 8mm in direction N131°. Solid lines show the traces viewed from the sonde-axis (azimuths θ'), broken lines from the borehole-axis (azimuths θ).